Lysosomes drive the piecemeal removal of mitochondrial inner membrane

https://doi.org/10.1038/s41586-024-07835-w

Received: 5 March 2023

Accepted: 16 July 2024

Akriti Prashar[1,6], Claudio Bussi[2,7,8], Antony Fearns[2,8], Mariana I. Capurro[1], Xiaodong Gao[1], Hiromi Sesaki[3], Maximiliano G. Gutierrez[2] & Nicola L. Jones[1,4,5] ✉

Mitochondrial membranes define distinct structural and functional compartments. Cristae of the inner mitochondrial membrane (IMM) function as independent bioenergetic units that undergo rapid and transient remodelling, but the significance of this compartmentalized organization is unknown[1]. Using super-resolution microscopy, here we show that cytosolic IMM vesicles, devoid of outer mitochondrial membrane or mitochondrial matrix, are formed during resting state. These vesicles derived from the IMM (VDIMs) are formed by IMM herniation through pores formed by voltage-dependent anion channel 1 in the outer mitochondrial membrane. Live-cell imaging showed that lysosomes in proximity to mitochondria engulfed the herniating IMM and, aided by the endosomal sorting complex required for transport machinery, led to the formation of VDIMs in a microautophagy-like process, sparing the remainder of the organelle. VDIM formation was enhanced in mitochondria undergoing oxidative stress, suggesting their potential role in maintenance of mitochondrial function. Furthermore, the formation of VDIMs required calcium release by the reactive oxygen species-activated, lysosomal calcium channel, transient receptor potential mucolipin 1, showing an interorganelle communication pathway for maintenance of mitochondrial homeostasis. Thus, IMM compartmentalization could allow for the selective removal of damaged IMM sections via VDIMs, which should protect mitochondria from localized injury. Our findings show a new pathway of intramitochondrial quality control.

Mitochondrial homeostasis is maintained by the hierarchical and coordinated activity of several quality control pathways. These include the removal of the entire organelle by processes such as mitophagy and mitocytosis, as well as mitochondrial remodelling by membrane-sorting pathways for removal of selective cargo (mitochondria-derived vesicles (MDVs), mitochondria-derived compartments, structures positive for mitochondrial outer membrane and mitochondria–lysosome-related organelles)[2–6].

The classical view of mitochondrial organization suggests that a uniform membrane potential ($\Delta\Psi_m$) exists across the entire organelle and that membrane depolarization leads to the clearance of damaged mitochondria by mitophagy[1]. However, recent findings have demonstrated that, unlike this equipotential model, each individual crista is an independent, highly dynamic anatomic and functional unit that maintains its own $\Delta\Psi_m$ independently of adjacent cristae[7,8]. The inner mitochondrial membrane (IMM) is subcompartmentalized into the inner boundary membrane (IBM), running parallel to the outer mitochondrial membrane (OMM), and the cristae, formed by IMM invaginations[9]. Cristae junctions separate cristae from the IBM and delineate specialized compartments in which are located the complexes needed for ATP generation by oxidative phosphorylation[9]. This compartmentalized IMM organization is speculated to prevent the spread of damage from one crista to the remainder of the organelle[7]. However, localized damage could still cause mitochondrial dysfunction if damaged and healthy membranes mix during mitochondrial fusion, or if reactive oxygen species (ROS) produced by impaired cristae damage mitochondrial DNA (mtDNA). Therefore, we hypothesized that mechanisms must exist that selectively remove impaired sections of the IMM without causing damage to the entire organelle. By studying the remodelling of mitochondrial membranes using super-resolution microscopy, we discovered the presence of distinct, cytosolic IMM-derived vesicles that are encapsulated by lysosomes. Mechanistically, these vesicles form when the IMM herniates through voltage-gated anion channel (VDAC) pores in the OMM and is engulfed by lysosomes in a microautophagy-like process, needing the endosomal sorting complex required for transport (ESCRT) machinery. Our findings show that IMM compartmentalization can facilitate the selective removal of damaged IMM sections, thereby serving as an intramitochondrial quality control mechanism.

Cells form VDIMs at steady state

To study the different mitochondrial compartments we labelled mitochondria in immortalized mouse embryonic fibroblasts (MEFs) at steady state with the mitochondria-selective dye nonyl acridine orange (NAO) that partitions to the IMM[7], along with matrix-targeted mito-BFP and OMM-localized mApple-TOM20. We observed distinct

---

[1] Cell Biology Program, The Hospital for Sick Children, Toronto, Ontario, Canada. [2] Host-Pathogen Interactions in Tuberculosis Laboratory, The Francis Crick Institute, London, UK. [3] Department of Cell Biology, Johns Hopkins University School of Medicine, Baltimore, MD, USA. [4] Division of Gastroenterology, Hepatology and Nutrition, The Hospital for Sick Children, Toronto, Ontario, Canada. [5] Departments of Paediatrics and Physiology, University of Toronto, Toronto, Ontario, Canada. [6] Present address: NHLBI, NIH, Bethesda, MD, USA. [7] Present address: School of Biological Sciences, Nanyang Technical University, Singapore, Singapore. [8] These authors contributed equally: Claudio Bussi, Antony Fearns. ✉e-mail: Nicola.jones@sickkids.ca

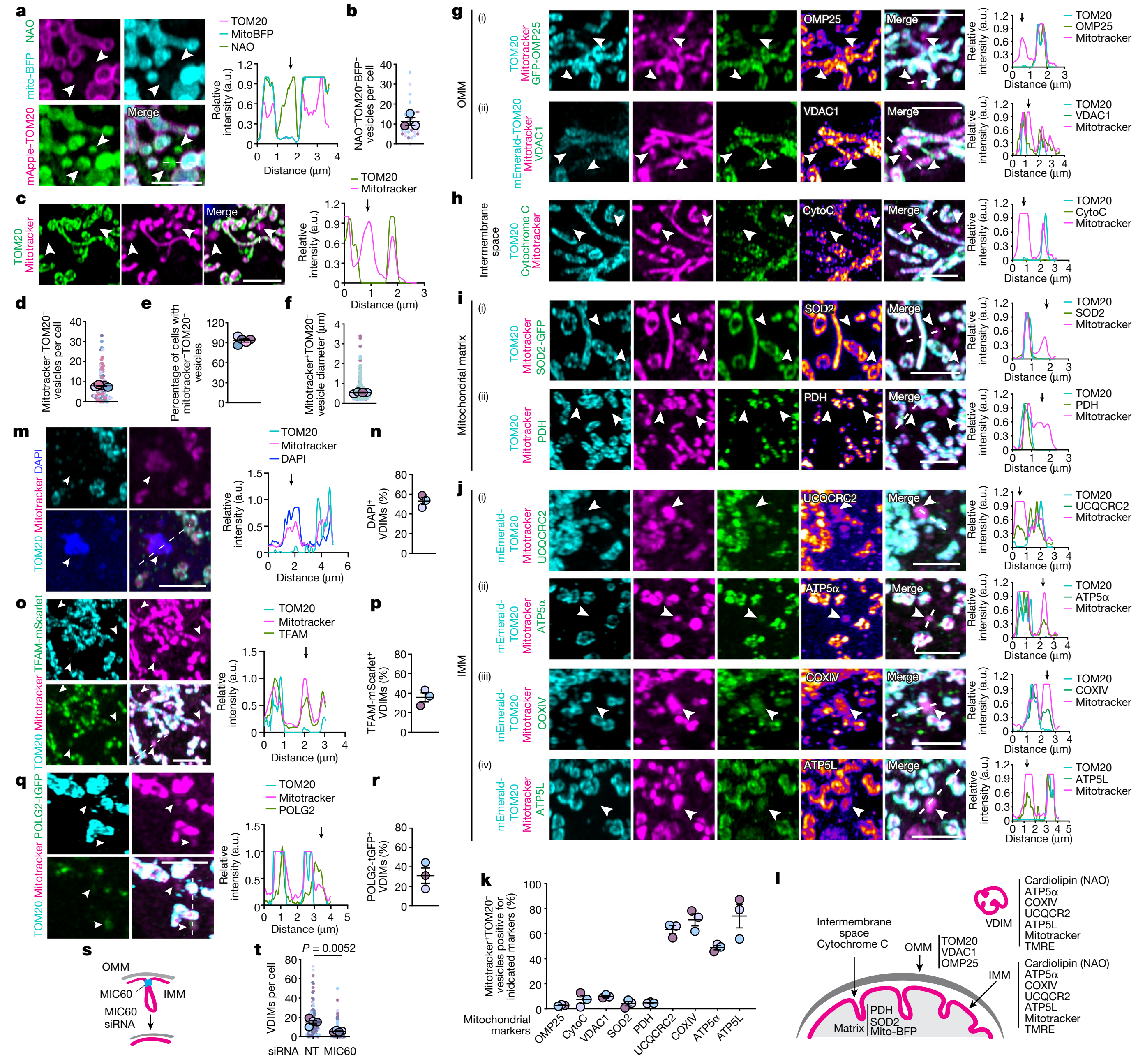

Fig. 1 | See next page for caption.

cytosolic NAO+ (IMM) vesicles lacking matrix or OMM (Fig. 1a,b and Extended Data Fig. 1a). These NAO+ vesicles were also detected using the additional IMM-localized probes tetramethylrhodamine ethyl ester (TMRE) and MitoTracker CMXRos[7] (herein referred to as mitotracker; Extended Data Fig. 1b–d). Because mitotracker is well retained following fixation, and the formation of these vesicles was affected by neither fixation conditions (Extended Data Fig. 2a), nor mitotracker concentration (Extended Data Fig. 2b), we utilized mitotracker and TOM20, which was absent from these vesicles (Fig. 1c and Extended Data Fig. 1e) to further investigate their formation.

At steady state over 90% of cells contained mitotracker+/TOM20− vesicles, with an average of 7.9 vesicles per cell and average diameter of around 0.5 µm (Fig. 1d–f). Importantly, these vesicles were present at resting state in all cell types tested (Extended Data Fig. 2c–g). We next excluded the possibility that these vesicles were membranes non-specifically labelled by mitotracker. Mitotracker did not localize with either endoplasmic reticulum- or Golgi-specific markers, Calnexin or GM130, respectively (Extended Data Fig. 2h,i). Furthermore, in cells in which mitochondria were severely depleted[10], mitotracker labelling was not detected (Extended Data Fig. 2j–l). Consistent with IMM labelling, mitotracker+/TOM20− vesicles contained makers from the IMM but lacked proteins localized at the OMM, mitochondrial matrix or intermembrane space (Fig. 1g–k and Extended Data Fig. 3a–i), confirming their IMM origin. We refer to these IMM-derived vesicles lacking markers from all other mitochondrial compartments as vesicles derived from the IMM (VDIMs) (Fig. 1l). A proportion of VDIMs contained mtDNA, as shown by labelling with the DNA-specific fluorescent dye DAPI, mtDNA-specific transcription factor A (TFAM) and DNA polymerase subunit gamma-2 (POLG2) (Fig. 1m–r and Extended Data Fig. 3j–l).

We reasoned that, if the compartmentalized organization of the IMM facilitates its selective removal by VDIMs, alteration of this organization should impede VDIM formation. The complex architecture of the IMM is regulated by the mitochondrial contact site and cristae-organizing system complex consisting of seven subunits, including MIC60, which

Fig. 1 | Selective sorting of IMM proteins into VDIMs. a, Cytosolic TOM20^{-}/NAO^{+}/mito-BFP^{-} vesicles (arrowheads) in MEFs expressing mito-BFP (cyan, matrix) and mApple-TOM20 (magenta, OMM), stained with NAO (green, IMM). Right, pixel intensity plot for dashed line; arrow indicates the vesicle. **b**, Number of TOM20^{-}/NAO^{+}/mito-BFP^{-} vesicles in experiments as in **a**; n = 336 vesicles, 30 cells, three experiments. **c**, Representative images of mitotracker^{+}/TOM20^{-} vesicles (arrowheads). Right, pixel intensity plot for dashed line; arrow indicates the vesicle. **d**,**e**, Quantification of number of mitotracker^{+}/TOM20^{-} vesicles (**d**, n = 824 vesicles, 104 cells, five experiments) and percentage of cells containing mitotracker^{+}/TOM20^{-} vesicles (**e**, n = 104 cells, five experiments) in experiments as in **c**. **f**, Size of mitotracker^{+}/TOM20^{-} vesicles in experiments as in **c**; n = 548 vesicles, 42 cells, four experiments. **g**, Absence of localization of OMM-localized proteins GFP-OMP25 (i, green) and VDAC1 (ii, green) with mitotracker^{+}/TOM20^{-} vesicles. **h**, Absence of localization of intermembrane space-localized cytochrome C (green) with mitotracker^{+}/TOM20^{-} vesicles. **i**, Absence of localization of mitochondrial matrix-localized proteins SOD2-GFP (i, green) and PDH (ii, green) with mitotracker^{+}/TOM20^{-} vesicles. **j**, Presence of IMM-localized proteins UCQCRC (i, green), ATP5α (ii, green), COXIV (iii, green) and ATP5L (iv, green) in mitotracker^{+}/TOM20^{-} vesicles in cells expressing m-Emerald-TOM20 (cyan). **k**, Percentage of mitotracker^{+}/TOM20^{-} vesicles positive for indicated mitochondrial markers from **g**–**j** (n = 349 vesicles, 30 cells, three experiments for OMP25; n = 282 vesicles, 31 cells, three experiments for VDAC1; n = 312 vesicles, 33 cells, three experiments for cyto C; n = 288 vesicles, 30 cells, three experiments for SOD2; n = 294 vesicles, 30 cells, three experiments for PDH; n = 286 vesicles, 29 cells, three experiments for UCQCRC2; n = 216 vesicles, 30 cells, three experiments for COXIV; n = 210 vesicles, 31 cells, three experiments for ATP5α; n = 267 vesicles, 30 cells, three experiments for ATP5L). **l**, Schematic showing mitochondrial markers analysed for their localization with mitotracker^{+}/TOM20^{-} vesicles. **m**–**r**, Presence of mtDNA in VDIMs. **m**, VDIMs (arrowheads) in cells stained with DAPI. Right, pixel intensity plot for dashed line; arrow indicates the vesicle. **n**, Percentage of VDIMs positive for DAPI in experiments as in **m** (n = 442 vesicles, 70 cells, three experiments). **o**, VDIMs (arrowheads) in cells expressing TFAM-mScarlet (green). Right, pixel intensity plot for dashed line. Arrow indicates the vesicle. **p**, Percentage of VDIMs positive for TFAM in experiments as in **o** (n = 484 vesicles, 30 cells, three experiments). **q**, VDIMs (arrowheads) in cells expressing POLG2-tGFP (green). Right, pixel intensity plot for dashed line; arrow indicates the vesicle. **r**, Percentage of VDIMs positive for POLG2 in experiments as in **q** (n = 347 vesicles, 30 cells, three experiments). **s**, Schematic illustrating the effect of silencing MIC60 on IMM organization. **t**, Number of VDIMs in cells treated with non-targeting (NT) or MIC60 small interfering RNA (n = 123 cells for NT, 121 cells for MIC60 siRNA, four experiments). **e**,**k**,**n**,**p**,**r**, Data shown are mean ± s.e.m. **b**,**d**,**f**,**t**, Mean ± s.e.m. represented by large circles, with individual data points from corresponding experiments shown in the same colours. Statistical analysis was performed using two-tailed Student's unpaired t-test. P values are indicated. **b**,**e**,**k**,**n**–**r**, Quantifications from Airyscan images. **g**–**j**, Pixel intensity plots for dashed lines are shown to the right. Rainbow pseudocoloured images for the indicated mitochondrial markers are shown. Representative images from three independent experiments are shown. Scale bars, 3 µm. a.u., arbitrary units.

is necessary for stabilization of the complex and maintenance of IMM organization and mitochondrial function[8,11]. In line with this reasoning, VDIM formation was significantly impaired in cells depleted of MIC60 (Fig. 1s,t and Extended Data Fig. 3m,n), indicating that IMM compartmentalization contributes to their formation and further supporting the findings that VDIMs arise from the IMM.

The large diameter of VDIMs (Fig. 1f and Extended Data Fig. 4a,b) suggested that they differ from MDVs, which have a diameter of 60–150 nm (refs. 12,13). Indeed, VDIM formation did not require the activity of dynamin-related protein 1 (DRP1) or mitochondrial RHO GTPase 1 (MIRO1), GTPases crucial for MDV formation[13] (Extended Data Fig. 4c–g). In addition, depletion of sorting nexin 9 (SNX9), which plays a role in the generation and lysosomal delivery of a subset of MDVs[14], did not alter VDIM formation (Extended Data Fig. 1h–j). Similarly, unlike mitochondria-derived compartments that also require DRP1 for their formation and are induced in response to amino acid stress[6,15], VDIMs were detectable at resting state. Lastly, in contrast to VDIMs, structures positive for mitochondrial outer membrane are defined as mitotracker^{-}/TOM20^{+} structures[3]. Taken together, these findings demonstrate that VDIMs represent distinct, newly identified structures that originate from the IMM.

VDIM formation for mitochondrial quality control

Given that VDIMs lacked both the mitochondrial matrix and OMM proteins, we speculated that they were formed from IMM sections selectively removed as part of a quality control mechanism. To determine whether VDIMs promote the selective removal of IMM during mitochondrial stress, we first assessed their formation in cells undergoing oxidative stress-mediated mitochondrial damage. Treatment with mitochondrial stressors increased—whereas treatment with antioxidants N-acetyl-L-cysteine (NAC) or mitochondria-targeted MitoTempo markedly reduced—VDIM formation (Fig. 2a–d and Extended Data Fig. 5a–c). We next assessed whether VDIMs contain damaged IMMs using the peroxidation-sensitive probe MitoCLox, which labels cardiolipin in the IMM[16,17]. Lipid peroxidation, as detected by an increase in green/red intensity (Extended Data Fig. 5d–f), indicated the presence of oxidized cardiolipin in the VDIMs, collectively supporting their role in mitochondrial maintenance.

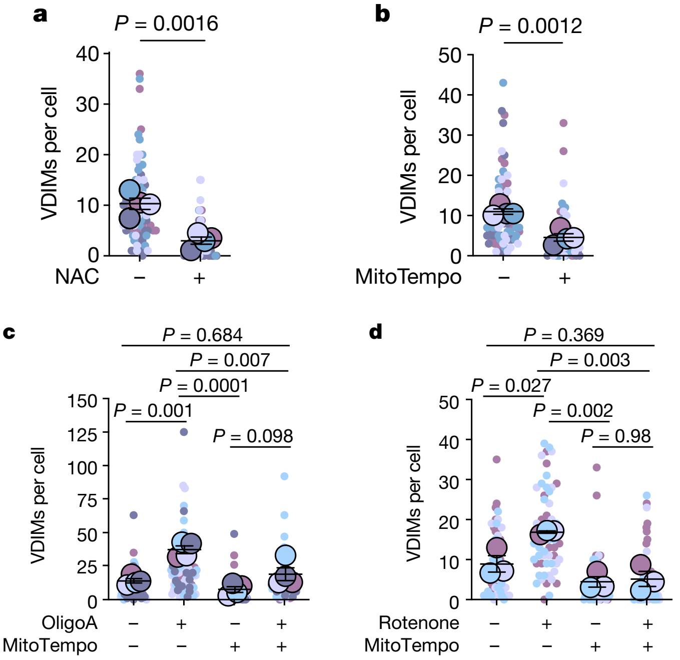

Fig. 2 | VDIM formation as an intramitochondrial quality control mechanism. a,**b**, Effect of scavenging ROS on VDIM formation. Cells were treated with either vehicle (–) and NAC (+) (**a**, n = 80 cells, four experiments) or mitoTempo (**b**, n = 81 cells, four experiments). **c**,**d**, Effect of oxidative damage on VDIM formation. **c**, Cells were treated with oligomycin A (oligoA), mitoTempo or oligoA + mitoTempo (n = 82 cells for vehicle, 81 cells for mitoTempo, 79 cells for oligoA, 79 cells for mitoTempo + oligoA, four experiments). **d**, Cells were treated with rotenone, mitoTempo or rotenone + mitoTempo (n = 60 cells for vehicle, 60 cells for mitoTempo, 62 cells for rotenone, 60 cells for rotenone + mitoTempo, three experiments). Data are mean ± s.e.m., represented by large circles, with individual data points from corresponding experiments shown in the same colours. Statistical significance was calculated using two-tailed Student's unpaired t-test (**a**,**b**) or one-way analysis of variance (ANOVA) followed by Tukey's multiple-comparison test (**c**,**d**). P values calculated are indicated.

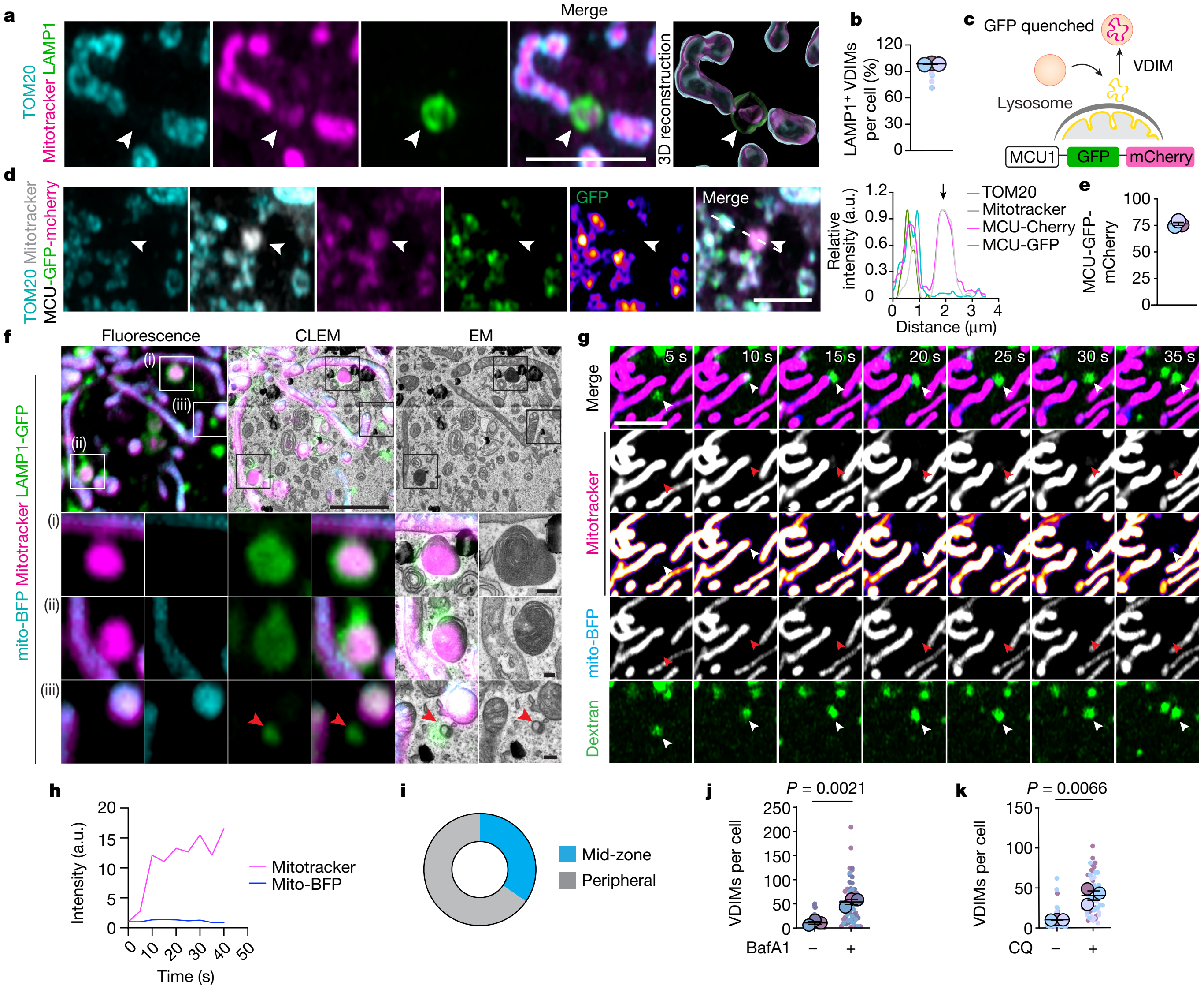

Fig. 3 | VDIMs are delivered to lysosomes for degradation. a, Localization of VDIMs in LAMP1⁺ lysosomes. Right, three-dimensional (3D) reconstruction; arrowheads indicate VDIMs. **b**, Number of LAMP1⁺ VDIMs in experiments as in **a** (*n* = 36 cells, three experiments). **c**, Schematic illustrating the loss of GFP fluorescence from lysosome-localized VDIMs in cells expressing MCU-GFP-mCherry. **d**, VDIMs in cells expressing MCU-GFP-mCherry; arrowheads indicate VDIMs retaining mCherry fluorescence with GFP fluorescence quenched; rainbow pseudocoloured GFP channel also shown. Right, pixel intensity plot for dashed line; arrow indicates the vesicle. **e**, Number of mCherry⁺/GFP⁻ VDIMs in experiments as in **d** (*n* = 330 vesicles, 26 cells, three experiments). **f**, CLEM analysis of cells expressing LAMP1-GFP (green) and mito-BFP (cyan), labelled with mitotracker (magenta). Bottom, higher magnifications of single *z* plane from indicated regions: i,ii, lysosome-localized VDIMs and presence of membrane whorls; iii, lysosome devoid of mitotracker-labelled membrane (arrowheads). **g**, Live-cell imaging sequence showing VDIM formation (arrowheads) in cells expressing mito-BFP (blue). Lysosomes were labelled with dextran (green) and mitochondria with mitotracker (magenta). **h**, Mean intensity of mitotracker and mito-BFP in the lysosome over time, from **g**. **i**, Representative data from two experiments showing the percentage of VDIMs forming at the mitochondrial mid-zone or periphery in experiments as in **g** (*n* = 52 events, ten cells). Blue indicates the midpoint and grey indicates the periphery. **j**,**k**, Number of VDIMs in cells with impaired lysosomes. Cells were treated with either bafilomycin A1 (BafA1) (**j**, *n* = 60 cells, three experiments) or chloroquine (CQ; **k**, *n* = 60 cells, three experiments). Data are mean ± s.e.m., represented by large circles, with individual data points from corresponding experiments shown in the same colours. Statistical analysis was performed using two-tailed Student's unpaired *t*-test. *P* values calculated are shown. EM, electron microscopy. Scale bars, 10 µm (**f**, top), 200 nm (**f**, bottom), 3 µm (**a**,**d**,**g**).

Removal of damaged mtDNA is crucial for the maintenance of mitochondrial homeostasis, and several pathways exist to eliminate damage DNA from mitochondria, including removal via BAX/BAK pores[18], VDAC pores[19,20], MDVs[21] and endosomal trafficking[22]. Given the association between mitochondrial nucleoids and the IMM, mtDNA is particularly sensitive to oxidative stress. Therefore, we considered that VDIM formation might represent a mechanism for mtDNA removal. Although a proportion of VDIMs contained mtDNA (Fig. 1m–r) and labelling for 8-OHdG showed that VDIMs contained oxidized DNA (Extended Data Fig. 5g,h), VDIM formation was not impaired in 143b rho0 cells lacking mtDNA[23] (Extended Data Fig. 5i,j), indicating that oxidized mtDNA was not the trigger for their formation.

Because our findings suggested that the formation of VDIM occurs as a quality control mechanism for IMM removal, we investigated whether VDIMs were destined for lysosomal degradation. As shown in Fig. 3a,b, Extended Data Fig. 6a and Supplementary Video 1, VDIMs were localized inside compartments labelled with the lysosomal marker LAMP1, indicating their delivery to the lysosomes. Next, we generated a fluorescent reporter for the IMM-localized protein MCU1 (MCU-GFP-mCherry), in which sensitivity of green fluorescent protein

(GFP) to low pH can be used to monitor the lysosomal localization of the protein of interest (Fig. 3c). As shown in Fig. 3d and Extended Data Fig. 6b, the probe localized to the mitochondria along with TOM20 and mitotracker. However, VDIMs lacked GFP but remained mCherry positive, demonstrating the probe's localization in an acidic compartment (Fig. 3d,e).

To confirm the lysosomal delivery of VDIMs we performed correlative light and electron microscopy (CLEM), which showed the presence of mitotracker$^+$/matrix$^-$ vesicles within lysosomes (Fig. 3f). These appeared as membrane whorls inside lysosomes in CLEM analysis. Of note, lysosomes devoid of mitotracker lacked these luminal membranes (Fig. 3f, Extended Data Fig. 6c and Supplementary Video 2).

Endocytic organelles, multivesicular bodies (MVBs), are characterized by the presence of intraluminal vesicles and membrane whorls generated from the invagination and budding of their limiting membrane[24]. To confirm that VDIMs were indeed lysosomal and not MVBs, we assessed their localization with MVB markers. In contrast to MVBs[24], CD63 and lysobiphosphatidic acid failed to localize with VDIMs (Extended Data Fig. 7a–d). In addition, VDIM formation did not depend on Arlb8 GTPase, which is required for lysosome–MVB fusion[25] (Extended Data Fig. 7e–i), further differentiating VDIM-containing lysosomes from MVBs.

Finally, we directly visualized the delivery of VDIMs to lysosomes by performing live-cell imaging of cells expressing mito-BFP (matrix), in which mitochondria were also labelled with mitotracker and lysosomes labelled with fluorescent dextran. Mitotracker$^+$/matrix$^-$ vesicles pinched off from mitochondria and were directly delivered into dextran-labelled lysosomes closely apposed to the mitochondrial surface (Fig. 3g, Extended Data Fig. 6d and Supplementary Videos 3 and 4). This transfer of mitotracker$^+$ vesicles was evident by the concomitant increase in mitotracker intensity inside the lysosome (Fig. 3h). Notably, sites of VDIM formation showed no preference for the mid-zone or periphery along a particular mitochondrion (Fig. 3i). This contrasts with the preferential peripheral fission observed for mitochondria delivered to lysosomes for degradation[26]. Similarly, if VDIMs represent remnants from partial proteolysis of mitochondria, inhibition of lysosomal function would cause a decrease in the number of VDIMs. However, treatment with bafilomycin A1 (BafA1) or chloroquine to inhibit lysosomal acidification and function resulted in an increase in the number of VDIMs (Fig. 3j,k and Extended Data Fig. 6e,f). These findings were not limited to TOM20, because localization of OMP25, PDH or SOD2 with VDIMs was not altered in BafA1-treated cells (Extended Data Fig. 6g–l). Collectively, these data confirmed that VDIMs were delivered to lysosomes for degradation and suggest that VDIM formation could represent a new intramitochondrial quality control pathway in response to localized IMM damage.

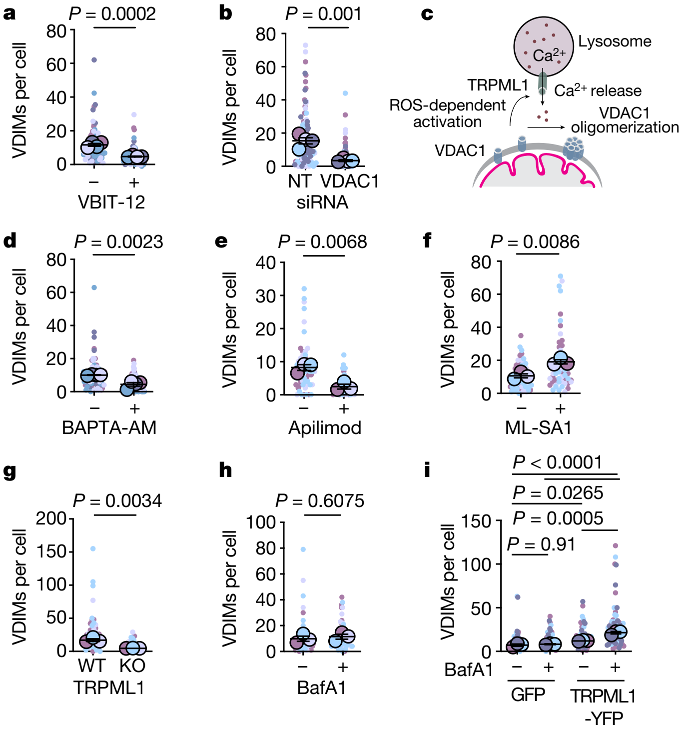

Fig. 4 | VDAC1 and lysosomal Ca^{2+} channel TRMPL1 mediate VDIM formation. **a**, Number of VDIMs in cells treated with VBIT-12 ($n = 81$ cells for vehicle, 83 for VBIT-12, four experiments). **b**, Number of VDIMs in cells treated with scrambled (NT) or VDAC1 siRNA ($n = 36$ cells, four experiments). **c**, Schematic illustrating mitochondria–lysosome cross-talk mediated by VDAC1 and TRPML1. **d**, Number of VDIMs in cells treated with vehicle (–) or BAPTA-AM ($n = 80$ cells, four experiments). **e**,**f**, Effect of TRPML1 activity on VDIM formation. Cells were treated with apilimod (**e**, $n = 60$ cells, three experiments) or ML-SA1 (**f**, $n = 60$ cells, three experiments). **g**–**i**, Effect of TRPML1 on VDIM formation. **g**, Number of VDIMs formed in *Trpml1*$^{-/-}$ (knockout, KO) and littermate WT MEFs ($n = 55$ cells, three experiments). **h**, VDIM formation in TRPML1 KO MEFs treated with vehicle (–) or BafA1 ($n = 62$ cells, three experiments). **i**, Rescue of VDIM formation in TRPML1 KO MEFs re-expressing TRPML1. TRPML1 KO MEFs were transiently transfected with GFP or TRPML1-YFP. Cells were treated with vehicle (–) or BafA1 (+) to facilitate accumulation of VDIMs ($n = 59$ for GFP + vehicle, 62 for GFP + BafA1, 60 for TRPML1-YFP + vehicle, 60 for TRPML1-YFP + BafA1, three experiments). Data are mean ± s.e.m., represented by large circles, with individual data points from corresponding experiments shown in the same colours. Statistical analysis was performed using either two-tailed Student's unpaired *t*-test (**a**,**b**,**d**–**h**) or one-way ANOVA followed by Tukey's multiple-comparison test (**i**). *P* values calculated are shown.

VDIMs form by mitochondria–lysosome cross-talk

We next dissected the pathway by which VDIMs were delivered to lysosomes. VDIM formation spared the remainder of the mitochondrial filament, suggesting that their formation had occurred without rupture of the OMM. The OMM-localized voltage-gated anion channel (VDAC) can oligomerize to form large pores, resulting in the release of mtDNA[20]. These pores, which can consist of up to 20 monomers[27,28], form in response to oxidative stress and increases in cytosolic calcium (Ca^{2+})[29]. Therefore, we investigated whether VDAC1 is needed for VDIM formation. Treatment with the VDAC inhibitor VBIT-12 (ref. 30) or silencing of VDAC1 expression precluded VDIM formation (Fig. 4a,b and Extended Data Fig. 8a–c), supporting a role of VDAC1 in VDIM formation. Interestingly, VDAC interacts with the lysosomal Ca^{2+} channel, transient receptor potential mucolipin1 (TRPML1)[31], which responds to mitochondrial ROS by releasing Ca^{2+} (ref. 32), which in turn can regulate mitochondrial function[33]. Given the proximity between mitochondria and lysosome during VDIM formation, we explored the role of the TRPML1–Ca^{2+}–VDAC axis in their formation (Fig. 4c). Treatment with the cell-permeable Ca^{2+} chelator BAPTA-AM resulted in a significant reduction in VDIM formation (Fig. 4d and Extended Data Fig. 8d). Similarly, impairment of TRPML1 activity by apilimod[34] reduced, whereas treatment with its agonist ML-SA1 (ref. 35) induced, VDIM formation (Fig. 4e,f and Extended Data Fig. 8e,f). Of note, targeting VDAC or TRPML1 did not alter the localization of OMP25 or PDH with VDIMs (Extended Data Fig. 8g–j).

We further confirmed the involvement of TRPML1-dependent Ca^{2+} release in VDIM formation by generating *Trpml1*$^{-/-}$ and littermate wild-type (WT) MEFs (Extended Data Fig. 8k). At steady state, VDIM formation was inhibited in *Trpml1*$^{-/-}$ MEFs (Fig. 4g and Extended Data Fig. 8l). Furthermore, compared with WT cells (Fig. 3j), *Trpml1*$^{-/-}$ cells failed to accumulate VDIMs in the presence of BafA1 (Fig. 4h and Extended Data Fig. 8m). This defect in VDIM formation was rescued following re-expression of TRPML1 in *Trpml1*$^{-/-}$ cells (Fig. 4i and Extended Data Fig. 8n). Taken together, these results illustrate that interorganelle

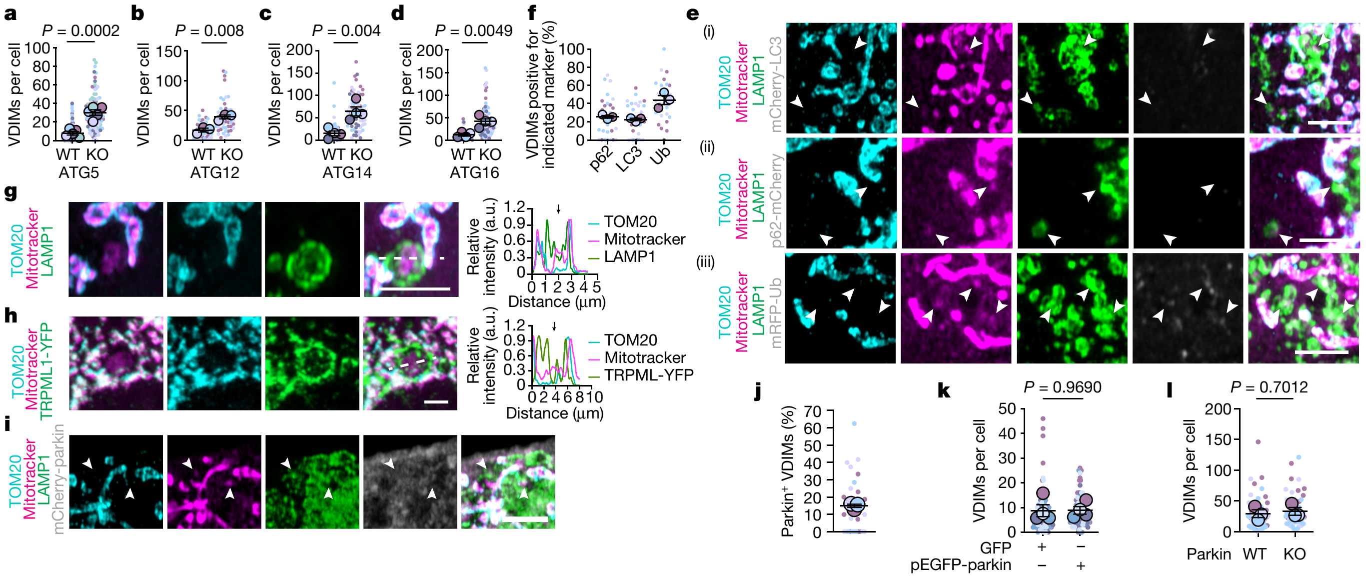

Fig. 5 | VDIMs form by engulfment of IMM by lysosomes in a microautophagy-like process. a–d, Number of VDIMs in *Atg5*$^{-/-}$ (KO) (**a**, n = 101 WT, 98 KO cells, five experiments), *Atg12*$^{-/-}$ (KO) (**b**, n = 40 WT, 46 KO cells, three experiments), *Atg14*$^{-/-}$ (KO) (**c**, n = 61 WT, 91 KO cells, four experiments) and *Atg16*$^{-/-}$ (KO) (**d**, n = 73 WT, 72 KO cells, four experiments) MEFs compared with those from littermate WT controls. **e**, Localization of VDIMs and indicated autophagy markers. Mitochondria in cells expressing (i) mCherry-LC3 (grey) (n = 264 vesicles, 29 cells, three experiments), (ii) p62-mCherry (grey) (n = 285 vesicles, 30 cells, three experiments) or (iii) mRFP-ubiquitin (mRFP-Ub; grey) (n = 264 vesicles, 30 cells, three experiments) labelled with mitotracker (magenta) and TOM20 (cyan) to identify VDIMs (arrowheads). **f**, Percentage of VDIMs positive for indicated autophagy markers in experiments as in **e** (n = 331 vesicles, 30 cells, three experiments for p62; n = 261 vesicles, 30 cells, three experiments for LC3; n = 394 vesicles, 31 cells, three experiments for Ub). **g**,**h**, Lysosome membrane LAMP1 (**g**) and TRPML1 vesicles (**h**) within the lumina of lysosomes containing VDIMs. Right, pixel intensity plot for dashed line; arrows indicate VDIMs. **i**, Absence of parkin localization with VDIMs (arrowheads) in cells expressing mCherry-parkin (grey). **j**, Percentage of VDIMs positive for parkin in experiments as in **i** (n = 240 vesicles, 28 cells, three experiments). **k**, Number of VDIMs in cells overexpressing GFP or pEGFP-parkin (n = 80 cells, four experiments). **l**, Number of VDIMs in *parkin*$^{-/-}$ (KO) MEFs compared with littermate WT control MEFs (n = 57 cells, three experiments). Data are mean ± s.e.m., represented by large circles, with individual data points from corresponding experiments shown in the same colours. **a**–**d**,**k**,**l**, Statistical analysis was performed using two-tailed Student's unpaired t-test. P values calculated are shown. Scale bars, 3 µm.

communication between mitochondria and lysosomes facilitates VDIM formation.

VDIMs form by ESCRT-mediated microautophagy

Delivery of cargo to lysosomes can occur indirectly by fusion of autophagosomes with lysosomes during macroautophagy[36]. Alternatively, lysosomes directly take up cargo by recognition of a KFERQ-like motif bearing cytosolic proteins during chaperone-mediated autophagy[37], or via microautophagy[38], in which invagination of lysosomal membrane sequesters cargo, followed by membrane scission leading to cargo internalization and the formation of intraluminal vesicles positive for lysosomal membrane proteins[39–42].

VDIM formation was not abrogated in cells lacking the core autophagy machinery components ATG5, ATG12, ATG14 and ATG16L1 (ref. 43) (Fig. 5a–d and Extended Data Fig. 9a), and the vesicles were generated by the same mechanism in the absence of ATG5 (Extended Data Fig. 9b–s). In addition, the canonical autophagy markers, p62 and LC3B[43,44] failed to localize with VDIMs (Fig. 5e,f and Extended Data Fig. 9t,u). Therefore, we ruled out the role of macroautophagy in VIDM formation. Notably, the absence of macroautophagy led to a greater number of VDIMs. Interestingly, 40% of VDIMs were positive for ubiquitin (Fig. 5e,f and Extended Data Fig. 9v). Recognition of ubiquitinated cargo is important for lysosomal microautophagy[45] and, as would be expected for membrane invagination during microautophagy, lysosomal transmembrane proteins were present in the lumina of lysosomes containing VDIMs (Fig. 5g,h, Extended Data Fig. 10a,b and Supplementary Video 5), altogether supporting a role of a microautophagy-like process in VDIM formation. The E3 ligase parkin is the most well-studied regulator of mitochondrial ubiquitination and mitophagy[46]. However, VDIMs lacked staining for parkin (Fig. 5i,j and Extended Data Fig. 10c), and neither the overexpression nor deletion of parkin altered their formation (Fig. 5k,l and Extended Data Fig. 10d,e), demonstrating that VDIM formation had occurred independently of parkin.

Because our findings indicated the presence of a mechanism of lysosomal sequestering of IMM and membrane scission, we examined whether the ESCRT machinery, which participates in membrane scission during microautophagy[47], was involved. In fixed cells, ESCRT complex proteins could be detected at potential sites of VDIM scission (Fig. 6a–e, Extended Data Fig. 10f–h and Supplementary Videos 6–8) where 'immature' VDIMs transition to 'mature' VDIMs, fully internalized by the lysosomes, as well as on 'mature' VDIMs. Notably, a greater percentage of immature VDIMs was positive for ESCRT proteins, indicative of their role in mediation of membrane scission for VDIM formation (Fig. 6e). Furthermore, live-cell imaging of cells expressing TSG101-GFP, labelled with mitotracker and fluorescent dextran (lysosomes), showed the recruitment of TSG101 at those sites where mitotracker^{+} vesicles pinched off and were engulfed by the lysosomes (Fig. 6f, Extended Data Fig. 10i and Supplementary Videos 9 and 10), thus indicating a role for ESCRTs in VDIM formation. The recruitment of ESCRT machinery required for membrane scission at the site of damaged plasma membrane and lysosomes is triggered by calcium sensing by apoptosis-linked gene 2 (ALG-2)[48]. Considering the role of calcium in VDIM formation, we wondered whether ALG-2 similarly regulates ESCRT recruitment for VDIM formation. Indeed, in support of a role for ALG-2 in ESCRT recruitment during VDIM formation, 35.4% of VDIMs were positive for ALG-2 (Fig. 6g,h and Extended Data Fig. 10j). If the ESCRT machinery facilitates membrane scission needed for the final step in VDIM formation, we surmised that its absence would result in stalled microautophagy, leading to partially formed VDIMs. Consistent with this, in cells in which expression of ESCRT protein TSG101 was

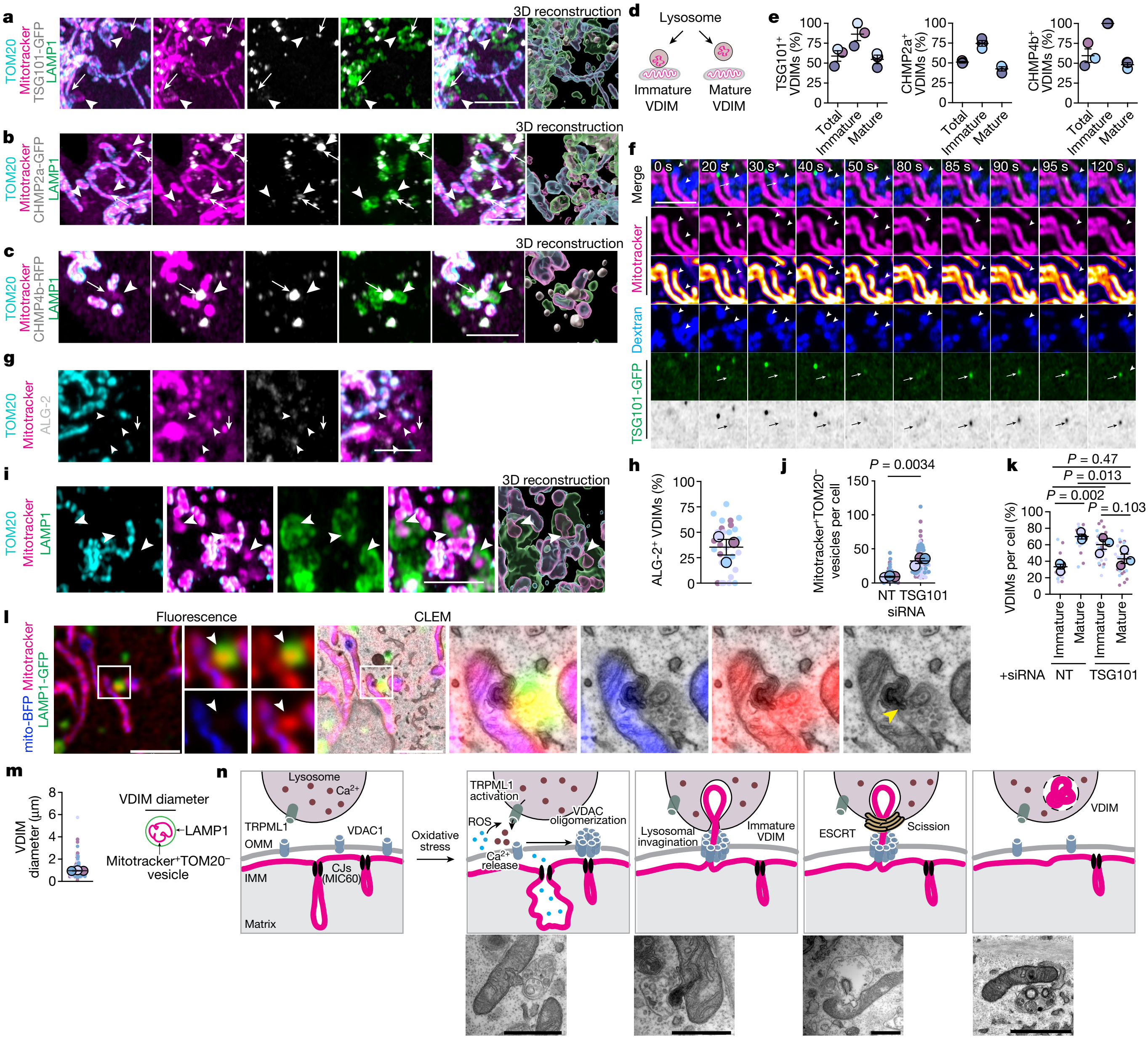

Fig. 6 | The ESCRT complex mediates VDIM formation. a–**c**, Localization of TSG101-GFP (**a**), CHMP2a-GFP (**b**) and CHMP4b-RFP (**c**) (grey) with VDIMs (arrowheads); arrows indicate ESCRT puncta. Right, 3D reconstruction. **d**, Schematic illustrating VDIM stages observed in fixed-cell imaging. **e**, Percentages of immature and mature VDIMs positive for indicated proteins in experiments as in **a**–**c** ($n = 31$ cells for TSG101, 30 cells for CHMP2a, 30 cells for CHMP4b, three experiments). **f**, Live-cell imaging sequence showing TSG101 recruitment at sites of VDIM scission. Images were acquired every 5 s; arrowheads indicate VDIMs and arrows indicate Tsg101 puncta ($n = 25$ events). **g**, ALG-2$^+$ (grey) VDIMs (arrowheads); arrow indicates an ALG-2$^-$ VDIM. **h**, Percentage of VDIMs positive for ALG-2 from experiments as in **g** ($n = 408$ vesicles, 29 cells, three experiments). **i**, Representative images showing impaired vesicle scission (arrowheads) following TSG101 depletion. Right, 3D reconstruction. **j**, Number of mitotracker$^+$/TOM20$^-$ vesicles following TSG101 depletion ($n = 71$ cells, three experiments). **k**, Percentage of immature and mature VDIMs following TSG101 depletion from **j**. **l**, CLEM analysis of cells expressing LAMP1-GFP (green) or mito-BFP (cyan) following TSG101 depletion (mitotracker depicted in magenta). Yellow arrowhead indicates the IMM herniating into the lysosome. **m**, Size distribution of VDIMs from Airyscan images ($n = 548$ vesicles, 42 cells, four experiments). Right, schematic illustrating the IMM encapsulated by a lysosome, forming a VDIM. **n**, Top, schematic illustrating the proposed mechanism of VDIM formation. Bottom, EM micrographs of TSG101-depleted cells from **l**, illustrating the different stages of VDIM formation. All data shown are from at least three independent experiments, with mean ± s.e.m. represented by large circles and with individual data points from corresponding experiments shown in the same colours. Scale bars, 200 nm. Statistical significance was calculated using either two-tailed Student's unpaired *t*-test (**j**) or one-way ANOVA followed by Tukey's multiple-comparison test (**k**). *P* values calculated are shown. Scale bars, 3 µm (**a**–**c**,**f**,**g**,**i**), 10 µm (**l**, left), 200 nm (**l**, right). CJ, cristae junction.

depleted, we observed internalization of mitotracker$^+$/TOM20$^-$ vesicles by lysosomes that appeared to remain attached to the mitochondrial filaments, indicating impaired scission (Fig. 6i, Extended Data Fig. 10l and Supplementary Video 11). This failure in scission required for VDIM formation, and the subsequent lack of lysosomal degradation of IMM fragments, resulted in an increase in the number of immature VDIMs present in these cells (Fig. 6j,k). CLEM analysis of TSG101-depleted cells clearly showed the IMM herniating into a lysosome, resembling an immature VDIM (Fig. 6l). These findings, along with the observation that VDIMs were always present within lysosomes (Fig. 3b), suggested that lysosomes are required for VDIM formation. Collectively, these data demonstrate that a microautophagy-like process mediated by the ESCRT machinery leads to the formation of VDIMs that are IMM sections encapsulated by lysosomes, ranging in size from 0.1 to 5.6 µm (Fig. 6m).

Alterations in crista size, shape and integrity are associated with several diseases including cancer and neurodegeneration[49]. However, the contribution of aberrant IMM dynamics to these processes is unknown. Here we provide a mechanistic description of a new pathway of intramitochondrial quality control, facilitated by IMM compartmentalization and mediated by IMM remodelling. We propose that ROS release by damaged cristae locally activates TRPML1 channels on lysosomes in proximity to mitochondria, leading to VDAC1 oligomerization. This oligomerization creates a pore in the OMM through which the damaged IMM fragment herniates and is directly taken up by the closely apposed lysosome. Given the close association between the IMM and mitochondrial nucleoids, we propose that mtDNA is taken up along with the herniating IMM. Next, ESCRT machinery-mediated membrane scission leads to their lysosomal internalization and the formation of VDIMs, resulting in the piecemeal removal of damaged IMM and sparing the remainder of the organelle (Fig. 6n).

Impairment of VDIM formation could lead to mitochondrial retention of damaged cristae. The consequent accumulation of oxidative damage would contribute to functional impairment of mitochondria (for example, mtDNA damage, impaired bioenergetics). Therefore, compartmentalized organization by itself could serve as an IMM quality control mechanism. In support of this rationale, the IMM protein mitochondrial fission process 1 (MTFP1) has recently been shown to selectively isolate damaged IMM subdomains and nucleoids to facilitate their removal via an autophagy-dependent process[50]. A better understating of the regulation of dynamic IMM organization, its remodelling and maintenance should lead to identification of potential therapeutic targets for mitochondrial diseases or other pathological processes in which mitochondrial homeostasis is disrupted.

Online content

Any methods, additional references, Nature Portfolio reporting summaries, source data, extended data, supplementary information, acknowledgements, peer review information; details of author contributions and competing interests; and statements of data and code availability are available at https://doi.org/10.1038/s41586-024-07835-w.

1. Kondadi, A. K., Anand, R. & Reichert, A. S. Cristae membrane dynamics – a paradigm change. *Trends Cell Biol.* **30**, 923–936 (2020).
2. Soubannier, V. et al. A vesicular transport pathway shuttles cargo from mitochondria to lysosomes. *Curr. Biol.* **22**, 135–141 (2012).
3. Li, X. et al. Mitochondria shed their outer membrane in response to infection-induced stress. *Science* **375**, eabi4343 (2022).
4. Jiao, H. et al. Mitocytosis, a migrasome-mediated mitochondrial quality-control process. *Cell* **184**, 2896–2910 (2021).
5. Ma, X. Mitochondria-lysosome-related organelles mediate mitochondrial clearance during cellular dedifferentiation. *Cell Rep.* **42**, 113291 (2023).
6. Hughes, A. L., Hughes, C. E., Henderson, K. A., Yazvenko, N. & Gottschling, D. E. Selective sorting and destruction of mitochondrial membrane proteins in aged yeast. *eLife* **5**, e13943 (2016).
7. Wolf, D. M. et al. Individual cristae within the same mitochondrion display different membrane potentials and are functionally independent. *EMBO J.* **38**, e101056 (2019).
8. Kondadi, A. K. et al. Cristae undergo continuous cycles of membrane remodelling in a MICOS-dependent manner. *EMBO Rep.* **21**, e49776 (2020).
9. Cogliati, S., Enriquez, J. A. & Scorrano, L. Mitochondrial cristae: where beauty meets functionality. *Trends Biochem. Sci.* **41**, 261–273 (2016).
10. Correia-Melo, C., Ichim, G., G Tait, S. W. & Passos, F. Depletion of mitochondria in mammalian cells through enforced mitophagy. *Nat. Protoc.* **12**, 183–194 (2016).
11. Stephan, T. et al. MICOS assembly controls mitochondrial inner membrane remodeling and crista junction redistribution to mediate cristae formation. *EMBO J.* **39**, e104105 (2020).
12. Sugiura, A., McLelland, G., Fon, E. A. & McBride, H. M. A new pathway for mitochondrial quality control: mitochondrial-derived vesicles. *EMBO J.* **33**, 2142–2156 (2014).
13. König, T. et al. MIROs and DRP1 drive mitochondrial-derived vesicle biogenesis and promote quality control. *Nat. Cell Biol.* **23**, 1271–1286 (2021).
14. Matheoud, D. et al. Parkinson's disease-related proteins PINK1 and Parkin repress mitochondrial antigen presentation. *Cell* **166**, 314–327 (2016).
15. Schuler, M. H. et al. Mitochondrial-derived compartments facilitate cellular adaptation to amino acid stress. *Mol. Cell* **81**, 3786–3802 (2021).
16. Lyamzaev, K. G. et al. MitoCLox: a novel mitochondria-targeted fluorescent probe for tracing lipid peroxidation. *Oxid. Med. Cell. Longev.* **2019**, 9710208 (2019).
17. Lyamzaev, K. G. et al. Novel fluorescent mitochondria-targeted probe MitoCLox reports lipid peroxidation in response to oxidative stress *in vivo*. *Oxid. Med. Cell. Longev.* **2020**, 3631272 (2020).
18. McArthur, K. et al. BAK/BAX macropores facilitate mitochondrial herniation and mtDNA efflux during apoptosis. *Science* **359**, eaao6047 (2018).
19. Xian, H. et al. Oxidized DNA fragments exit mitochondria via mPTP- and VDAC-dependent channels to activate NLRP3 inflammasome and interferon signaling. *Immunity* **55**, 1370–1385 (2022).
20. Kim, J. et al. VDAC oligomers form mitochondrial pores to release mtDNA fragments and promote lupus-like disease. *Science* **366**, 1531–1536 (2019).
21. Zecchini, V. et al. Fumarate induces vesicular release of mtDNA to drive innate immunity. *Nature* **615**, 499–506 (2023).
22. Newman, L. E. et al. Mitochondrial DNA replication stress triggers a pro-inflammatory endosomal pathway of nucleoid disposal. *Nat. Cell Biol.* **26**, 194–206 (2024).
23. D'Aco, K. E. et al. Mitochondrial tRNA(Phe) mutation as a cause of end-stage renal disease in childhood. *Pediatr. Nephrol.* **28**, 515–519 (2013).
24. Piper, R. C. & Katzmann, D. J. Biogenesis and function of multivesicular bodies. *Annu. Rev. Cell Dev. Biol.* **23**, 519–547 (2007).
25. Shelke, G. V., Williamson, C. D., Jarnik, M. & Bonifacino, J. S. Inhibition of endolysosome fusion increases exosome secretion. *J. Cell Biol.* **222**, e202209084 (2023).
26. Kleele, T. et al. Distinct fission signatures predict mitochondrial degradation or biogenesis. *Nature* **593**, 435–439 (2021).
27. Hoogenboom, B. W., Suda, K., Engel, A. & Fotiadis, D. The supramolecular assemblies of voltage-dependent anion channels in the native membrane. *J. Mol. Biol.* **370**, 246–255 (2007).
28. Gonçalves, R. P., Buzhynskyy, N., Prima, V., Sturgis, J. N. & Scheuring, S. Supramolecular assembly of VDAC in native mitochondrial outer membranes. *J. Mol. Biol.* **369**, 413–418 (2007).
29. Keinan, N., Tyomkin, D. & Shoshan-Barmatz, V. Oligomerization of the mitochondrial protein voltage-dependent anion channel is coupled to the induction of apoptosis. *Mol. Cell. Biol.* **30**, 5698–5709 (2010).
30. Shteinfer-Kuzmine, A. et al. Targeting the mitochondrial protein VDAC1 as a potential therapeutic strategy in ALS. *Int. J. Mol. Sci.* **23**, 9946 (2022).
31. Peng, W., Wong, Y. C. & Krainc, D. Mitochondria-lysosome contacts regulate mitochondrial Ca2^{+} dynamics via lysosomal TRPML1. *Proc. Natl Acad. Sci. USA* **117**, 19266–19275 (2020).
32. Zhang, X. et al. MCOLN1 is a ROS sensor in lysosomes that regulates autophagy. *Nat. Commun.* **7**, 12109 (2016).
33. Rossi, A., Pizzo, P. & Filadi, R. Calcium, mitochondria and cell metabolism: a functional triangle in bioenergetics. *Biochim. Biophys. Acta Mol. Cell. Res.* **1866**, 1068–1078 (2019).
34. Dayam, R. M., Saric, A., Shilliday, R. E. & Botelho, R. J. The phosphoinositide-gated lysosomal Ca^{2+} channel, TRPML1, is required for phagosome maturation. *Traffic* **16**, 1010–1026 (2015).
35. Chen, C. C. et al. A small molecule restores function to TRPML1 mutant isoforms responsible for mucolipidosis type IV. *Nat. Commun.* **5**, 4681 (2014).
36. Dikic, I. & Elazar, Z. Mechanism and medical implications of mammalian autophagy. *Nat. Rev. Mol. Cell Biol.* **19**, 349–364 (2018).
37. Kaushik, S. & Cuervo, A. M. The coming of age of chaperone-mediated autophagy. *Nat. Rev. Mol. Cell Biol.* **19**, 365–381 (2018).
38. Wang, L., Klionsky, D. J. & Shen, H. M. The emerging mechanisms and functions of microautophagy. *Nat. Rev. Mol. Cell Biol.* **24**, 186–203 (2023).
39. Müller, O. et al. Autophagic tubes: vacuolar invaginations involved in lateral membrane sorting and inverse vesicle budding. *J. Cell Biol.* **151**, 519–528 (2000).
40. Oku, M. et al. Evidence for ESC RT- and clathrin-dependent microautophagy. *J. Cell Biol.* **216**, 3263–3274 (2017).
41. Omari, S. et al. Noncanonical autophagy at ER exit sites regulates procollagen turnover. *Proc. Natl Acad. Sci. USA* **115**, E10099–E10108 (2018).
42. Lee, C., Lamech, L., Johns, E. & Overholtzer, M. Selective lysosome membrane turnover is induced by nutrient starvation. *Dev. Cell* **55**, 289–297 (2020).
43. Bento, C. F. et al. Mammalian autophagy: how does it work? *Annu. Rev. Biochem.* **85**, 685–713 (2016).
44. Pickles, S., Vigi, P. & Youle, R. J. Current biology review mitophagy and quality control mechanisms in mitochondrial maintenance. *Curr. Biol.* **28**, R170–R185 (2018).
45. Kuchitsu, Y. & Taguchi, T. Lysosomal microautophagy: an emerging dimension in mammalian autophagy. *Trends Cell Biol.* **34**, 606–616 (2023).
46. Palikaras, K., Lionaki, E. & Tavernarakis, N. Mechanisms of mitophagy in cellular homeostasis, physiology and pathology. *Nat. Cell Biol.* **20**, 1013–1022 (2018).
47. Vietri, M., Radulovic, M. & Stenmark, H. The many functions of ESCRTs. *Nat. Rev. Mol. Cell Biol.* **21**, 25–42 (2020).
48. Scheffer, L. L. et al. Mechanism of Ca2^{+}-triggered ESCRT assembly and regulation of cell membrane repair. *Nat. Commun.* **5**, 5646 (2014).
49. Huang, C., Deng, K. & Wu, M. Mitochondrial cristae in health and disease. *Int. J. Biol. Macromol.* **235**, 123755 (2023).
50. Tábara, L. C. et al. MTFP1 controls mitochondrial fusion to regulate inner membrane quality control and maintain mtDNA levels. *Cell* **187**, 3619–3637 (2024).

Methods

Reagents

NAO (Invitrogen, catalogue no. A1372) was used at 100 nM for 2 h. MitoCLox (Lumiprobe, catalogue no. 3549) was used at 200 nM for 1 h. Bafilomycin A1 (Cayman Chemicals, catalogue no. 11038) was used at 50 nM for 24 h. NAC (Sigma, catalogue no. A7250) was used at 5 mM for 24 h. MitoTempo (Sigma, catalogue no. SM10737) was used at 50 μM for 24 h. Oligomycin (Santa Cruz, catalogue no. sc201551) was used at 10 μM for 24 h. Rotenone (abcam, catalogue no. ab143145) was used at 10 μM for 24 h. VBIT-12 (Cayman Chemicals, catalogue no. 31445) was used at 10 μM for 24 h. ML-SA1 (Sigma, catalogue no. SML0627) was used at 20 μM for 24 h. BAPTA-AM (ThermoFisher, catalogue no. B1205) was used at 10 μM for 24 h. MitoTracker CMXRos (ThermoFisher, catalogue no. M7512) and MitoTracker DeepRed (ThermoFisher, catalogue no. M22426) were used at 100 nM for 15 min. Dextran Cascade blue and Dextran 488 were obtained from ThermoFisher (catalogue nos. D1796 and D22910, respectively). All primers used were obtained from Integrated DNA Technologies.

Plasmids and transfection

Mito-BFP was a gift from G. Voeltz (Addgene plasmid no. 49151), pDEST47-MCU-GFP was a gift from V. Mootha (Addgene plasmid no. 31732), LAMP1-GFP was a gift from R. Vale (Addgene plasmid no. 16290), TRPML1-YFP was a gift from C. Montell (Addgene plasmid no. 18826), CHMP2A_GFP_N_term was a gift from D. Gerlich (Addgene plasmid no. 31805) and pLNCX2-mCherry-CHMP4B was a gift from S. Simon (Addgene plasmid no. 116923). pEGFP-parkin was a gift from E. Fon (Addgene plasmid no. 45875), mCherry-DRP1 was a gift from G. Voeltz (Addgene plasmid no. 49152), mCherry-parkin was a gift from R. Youle (Addgene plasmid no. 23956) and TFAM-mScarlet was a gift from S. Tait (Addgene plasmid no. 129573). POLG2-tGFP was sourced from OriGene (catalogue no. RG203462). TSG101-GFP, described in ref. 51, was provided by S. Grinstein (The Hospital for Sick Children, Toronto, Canada). GFP-ARL8b, GFP-ARL8b-DN[52] and p62-mCherry[53] were provided by J. Brummell (Hospital for Sick Children, Toronto, Canada) and have previously been described. mApple-TOM20, mCherry-LC3, SOD2-GFP and GFP-Ub were generously provided by P. Kim (The Hospital for Sick Children, Toronto) and have previously been described[54–57].

MCU-GFP-mCherry was made for this study.

The mCherry insert was amplified from mCherry-DRP1 and subcloned into pDEST47-MCU-GFP using the In-Fusion protocol from TaKaRa Bio (catalogue no. 638954).

Insert F, 5′-GACGAGCTGTACAAGATGGTGAGCAAGGGCGAGG-3′
Insert R, 5′-TTAAACTTATCATTAACTTGTACAGCTCGTCCATGCC-3′
Vector F, 5′-TAATGATAAGTTTAAACGGGGGAGG-3′
Vector R, 5′-CTTGTACAGCTCGTCCATGCC-3′

In all cases, cells were analysed following overnight transfection with indicated plasmids using transfection reagent FuGENE-HD (Promega, catalogue no. E2311).

Cell culture

AGS, HeLa, ModeK and Cos-1 cells were sourced from the American Type Culture Collection. NCI-H292 cells, originally from the American Type Culture Collection, were generously provided by M. Terebiznik (University of Toronto at Scarborough, Toronto, Canada). *Drp1*$^{-/-}$ and WT littermate control MEFs have previously been defined[58]. *parkin*$^{-/-}$ and WT littermate control MEFs have previously been described[59]. *Atg5*$^{-/-}$ and control MEFs were provided by N. Mizushima (University of Tokyo). *Atg14*$^{-/-}$, *Atg16L1*$^{-/-}$ and corresponding WT littermate controls were generously provided by T. Yoshimori (Osaka University, Japan) and have previously been described[60]. MEFs and HeLa and Cos-1 cells were cultured in DMEM, 2 mM L-glutamine and non-essential amino acids supplemented with 10% fetal bovine serum (FBS) at 37 °C with 5% CO_2. NCI-H292 cells were cultured in RPMI-1640 medium and 2 mM L-glutamine supplemented with 10% FBS. AGS cells were cultured in Ham's F-12 culture medium and 2 mM L-glutamine supplemented with 10% FBS. HeLa cells stably expressing Mito-dsRED and EGFP-parkin were generously provided by J. Brummell (Hospital for Sick Children, Toronto, Canada) and have previously been described[61]. Previously described[23] 143b ρ0 and control cells were provided by N. Sondheimer (Hospital for Sick Children, Toronto) and were cultured in DMEM supplemented with 10% FBS, pyruvate and 50 μg ml^{-1} uridine. Cells were negative for mycoplasma contamination.

Generation of *Trpml1*$^{-/-}$ MEFs

Trpml1 heterozygous mice were obtained from S. Slaugenhaupt (Massachusetts General Hospital, Harvard Medical School) and bred to obtain *Trpml1*$^{-/-}$ and WT littermates.

MEFs were generated as described previously[62]. Briefly, embryos were harvested roughly 14 days following the appearance of a copulation plug. Tissue was cut into 1–2 mm pieces and digested in 0.25% trypsin-EDTA at 37 °C for 10 min, pipetted up and down several times and incubated at 37 °C for an additional 5 min. Tissue suspension was added to MEF culture medium (DMEM + 10% FBS/2 mM L-glutamine/1× penicillin-streptomycin), larger tissue fragments allowed to settle and the supernatant consisting of single cells was transferred to a T75 flask. Once confluent, cells were serial passaged every 5 days for several weeks. Immortalized MEFs were obtained at passage 20.

TRPML1 gene knockout from MEFs was confirmed by PCR using the following primers:

WT forward, 5′-TGA GGA GAG CCA AGC TCA TT-3′
WT reverse, 5′-TCA TCT TCC TGC CTC CAT CT-3′
NeoR, 5′-TGG CTG GAC GTA AAC TCC TC-3′

siRNA knockdown

Non-targeting siRNA (ON TARGETplus SMARTpool D-001810-10-05), siRNA targeting *Tsg101* (L-049922-01-0005), siRNA targeting *Vdac1* (L047345-00-0005), siRNA targeting *Mic60*/IMMT (L-046765-01-0005), siRNA targeting *Miro1* (L-063998-01-0005) and siRNA targeting *Snx9* (L-057505-01-0005) were obtained from Dharmacon (Horizon Discovery). Following overnight plating, 25 nM of each siRNA was added for 48 h. Media were removed and an additional 25 nM of each siRNA was added for 24 h. Cells were either lysed for immunoblot analysis or fixed in 4% paraformaldehyde for imaging, as described below. Knockdown was performed using Dharmafect transfection reagent (Dharmacon, catalogue no. T-2001-01, Horizon Discovery).

Depletion of mitochondria

Mitochondria were depleted following a previously described protocol[10]. Briefly, HeLa cells stably expressing mito-dsRed and eGFP-parkin[61] were treated with 12.5 μM carbonyl cyanide m-chlorophenylhydrazone (CCCP) every 12 h for 72 h. Expression of mitochondrial proteins was assessed by immunoblotting and immunofluorescence.

SDS–polyacrylamide gel electrophoresis and immunoblotting

At the indicated times, cells were lysed in RIPA buffer containing protease inhibitors for 20 min on ice. Lysates were denatured with Lammeli sample buffer containing 2-mercaptoethanol, boiled for 10 min and proteins resolved by SDS–polyacrylamide gel electrophoresis and transferred to nitrocellulose membranes (BioRad). Membranes were blocked with 5% non-fat milk in Tris-buffered saline with 0.1% Tween-20 (TBS-T) for 1 h at room temperature. Membranes were incubated with primary antibody at an appropriate dilution in blocking solution overnight at 4 °C. Membranes were washed three times for 10 min each with TBS-T and incubated with secondary antibodies in blocking solution for 1 h at room temperature. Following washes (three times for 10 min each with TBS-T), membranes were treated with ECL (Santa Cruz). Immunoblot visualization and densitometry analyses were performed using a Li-Cor Odyssey Fc imaging system and Image Studio.

The following antibodies were used for immunoblot analysis in this study: β-actin (1:5,000, Sigma-Aldrich, catalogue no. A5411), tsg101 (1:1,000, abcam, catalogue no. ab83), Vdac1 (1:1,000, no. ab154856, abcam), mic60 (anti-mitofilin) (1:1,000, Proteintech, catalogue no. 10179-1), anti-Opa1 (1:1,000, Proteintech, catalogue no. 27733-1-AP), horseradish peroxidase-conjugated goat anti-rabbit (1:5,000, Cedar lane, catalogue no. 111-035-144) and horseradish peroxidase-conjugated goat anti-mouse (1:5,000, Cedar lane, catalogue no. 115-035-003). Unless stated otherwise, all immunoblots shown are representative of at least three biological replicates.

Immunofluorescence

Cells cultured on glass coverslips were fixed overnight in 4% paraformaldehyde (Electron Microscopy Sciences) in 1× PBS at 4 °C. Following three washes in 1× PBS, cells were permeabilized with ice-cold methanol for 5 min, washed and blocked in 5% bovine serum albumin in PBS for 1 h at room temperature. Cells were incubated with primary antibodies diluted in blocking solution for 1 h at room temperature. Following three washes with PBS, secondary antibody incubations (1:1,000) were performed for 1 h at room temperature in blocking solution followed by nuclear staining with DAPI (5 μg ml^{-1}). Coverslips were mounted using Dako Fluorescence Mounting Media (Agilent Technologies).

The following primary antibodies were used for immunofluorescence analysis: anti-TOM20 (Proteintech, catalogue no. 11802-1-AP, 1:500), anti-cytochrome C (abcam, catalogue no. ab110325, 1:500), anti-PDH (abcam, catalogue no. ab110333, 1:500), anti-ATP5L (Proteintech, catalogue no. 16483, 1:500), anti-ATP5α (abcam, catalogue no. ab14748, 1:500), anti-VDAC1 (abcam, catalogue no. ab154856, 1:500), anti-COXIV (Proteintech, catalogue no. 11242-1-AP, 1:500), anti-UCQCRC2 (Proteintech, catalogue no. 14742-1-AP, 1:500), anti-8OHdG (Santa Cruz, catalogue no. 393871, 1:100), anti-CD63 (abcam, catalogue no. ab8219, 1:100), anti-LBPA (Echelon Biosciences, catalogue no. z-PLBPA, 1:500) and anti-ALG-2 (Proteintech, catalogue no. 12303-1-AP, 1:100). The following secondary antibodies were used for immunofluorescence analysis at 1:1,000 dilution: goat anti-rabbit Alexa 647 (Invitrogen, catalogue no. A21244), donkey anti-rabbit Alexa 405 (Invitrogen, catalogue no. A48258), goat anti-rabbit Alexa 488 (Invitrogen, catalogue no. A11011), goat anti-mouse Alexa 488 (Invitrogen, catalogue no. 11029), goat anti-mouse Alexa 647 (Invitrogen, catalogue no. A21235) and goat anti-rat Alexa 647 (Invitrogen, catalogue no. A21247).

For Airyscan imaging, cells fixed with 4% paraformaldehyde (4 °C, overnight) were quenched with 50 mM ammonium chloride for 10 min and washed with 1× PBS + 5% FBS. Cells were permeabilized for 5 min with ice-cold methanol and blocked in 1× PBS + 10% FBS for 1 h at room temperature. Cells were incubated with the indicated primary antibodies diluted in blocking solution for 1 h at room temperature and washed with 1× PBS + 5% FBS, followed by incubation with secondary antibodies (1:2,000), washing and mounting onto slides.

Microscopy

Unless stated otherwise, all fluorescent micrographs shown are high-resolution Airyscan images; time-lapse imaging was performed with a Zeiss LSM880 Airyscan confocal incorporating a ×63/1.4 numerical aperture PlanApo objective. Spinning-disc confocal images were acquired with a ×63/1.4 numerical aperture objective using a Quorum spinning-disc confocal microscope, consisting of an inverted fluorescence microscope (DMI6000B, Leica), an EM-CCD camera (Hamamatsu Photonics) and spinning-disc confocal scan head. The equipment was controlled by Volocity acquisition software (PerkinElmer). *Z*-stacks obtained were 300 nm apart.

For live-cell imaging, cells were plated on glass coverslips and transfected with mito-BFP overnight. For labelling of lysosomes, cells were incubated overnight with either dextran 488 (25 μg ml^{-1}) or Dextran Cascade blue (25 μg ml^{-1}), washed and chased for an additional 3–5 h in full media before imaging. Fifteen minutes before live-cell imaging, cells were incubated with 100 nM MitoTracker CMXRos in full media at 37 °C. Media were removed and cells washed with dye-free media before transfer to a prewarmed microscope stage. High-resolution Airyscan images were acquired using a ×63 oil DIC M27 objective every 5 s. Before analysis, raw image files were automatically processed into deconvoluted Airyscan images using Zen software (Zeiss).

For analysis of lipid peroxidation, cells transfected with mito-BFP were incubated with MitoCLox followed by incubation with mitotracker DeepRed before imaging. Where indicated, cells were treated with 500 μM H_2O_2 for 30 min as positive control. Images were acquired using a Quorum spinning-disc confocal microscope with excitation at 491 and 561 nm.

Confocal imaging for CLEM experiments was performed using a Leica SP8 confocal microscope, on which *z*-stack slices were set at 200 nm.

CLEM. Plasmid DNA (LAMP1-GFP and mito-BFP) was electroporated into cells using the Neon system (Invitrogen). Cells were resuspended (5×10^6) in 100 μl of buffer R; 10 μl of cells 1 μg^{-1} plasmid DNA mix was aspirated into a Neon pipette and electroporated in electroporation buffer E at 1,350 V for 30 ms, with one pulse. Cells were then plated in glass-bottom, 35 mm MatTek dishes for confocal imaging and electron microscopy studies. For CLEM analysis of TSG101-depleted cells, cells were treated with TSG101 siRNA for 72 h before electroporation of plasmid DNA. Before fixation, cells were incubated with 100 nM MitoTracker DeepRed for 20 min at 37 °C. Samples were then fixed by the addition to the culture medium of a mixture of 8% paraformaldehyde in 200 mM HEPES buffer (v/v) with incubation at room temperature for 15 min, followed by replacement with 4% paraformaldehyde in 100 mM HEPES for 30 min before imaging by confocal microscopy. Cells were imaged on a Leica SP8 confocal microscope using a ×63 objective (oil, 1.4 numerical aperture) and *z*-stacks were acquired at 150 nm per slice (1,024 × 1,024 resolution). A substack containing the event of interest was acquired at 2,048 × 2,048 resolution for subsequent CLEM analysis. Following fluorescence imaging, samples were transferred to 1% glutaraldehyde in 100 mM HEPES buffer.

Resin embedding. Fluorescently imaged samples were processed for CLEM in a Biowave Pro (Pelco) using microwave energy and vacuum. Cells were twice washed in HEPES (Sigma-Aldrich, catalogue no. H0887) at 250 W for 40 s and postfixed using a mixture of 2% osmium tetroxide (Taab, catalogue no. O011) and 1.5% potassium ferricyanide (Taab, catalogue no. P018) (v/v) in equal ratio for 14 min at 100 W power (with/without vacuum of 20 inches Hg at 2 min intervals). Samples were washed twice with distilled water on the bench and twice again in the Biowave at 250 W for 40 s. Samples were stained with 1% aqueous uranyl acetate (Agar scientific, catalogue no. AGR1260A) in distilled water (w/v) for 14 min at 100 W power (with/without vacuum of 20 inches Hg at 2 min intervals) then washed using the same settings as before. Samples were dehydrated using a step-wise acetone series of 50, 75, 90 and 100% then washed four times in absolute acetone at 250 W for 40 s per step. Samples were infiltrated with a dilution series of 25, 50, 75 and 100% Durcupan ACM (Sigma-Aldrich, catalogue no. 44610) (v/v) resin to propylene oxide. Each step was for 3 min at 250 W power (with/without vacuum of 20 inches Hg at 30 s intervals). Samples were then cured for a minimum of 48 h at 60 °C.

Sample trimming and transmission electron micrograph acquisition. Referring to grid coordinates, the sample block was trimmed coarsely by a razor blade then finely trimmed using a 35° ultrasonic, oscillating diamond knife (DiATOME) set at a cutting speed of 0.6 mm s^{-1}, a frequency set by automatic mode and a voltage of 6.0 V on an ultramicrotome EM UC7 (Leica Microsystems) to remove all excess resin surrounding the region of interest (ROI). Images were acquired using a 120 kv Tecnai G2 Spirit BioTwin (FEI Co.) with a OneView Camera (Gatan).

CLEM image alignment. Fluorescent.LIF files were converted to tiff file format and linear adjustments made to brightness and contrast using FIJI (v.2.0.0-rc-69/1.52p). Images were aligned to electron microscopy micrographs with Icy 2.0.3.0 software (Institut Pasteur) using the ec-CLEM v.1.0.1.5 plug-in. No fewer than ten independent fiducials were chosen per alignment for two-dimensional image registration. When fiducial registration error was greater than that predicted, a non-rigid transformation (nonlinear transformation based on spline interpolation following an initial rigid transformation) was applied as previously described[63].

Image analysis

Quantification of VDIMs. Unless stated otherwise, all quantifications were performed on maximum-intensity projections of images acquired using a spinning-disc confocal microscope, using ImageJ (Fiji). OMM was labelled using anti-TOM20 antibodies, and mitochondrial IMM labelled using mitotracker. ROIs were selected around cells and duplicated, and a mask of each channel was generated. To do this, a manual threshold was applied to each channel and the 'erode' command was applied to the mitotracker channel and 'dilate' command applied to the TOM20 channel to expand the mask by one pixel. The TOM20 mask was subtracted from the mitotracker mask and the result used to measure the number and size of VDIMs with the 'Analyze particles' plug-in. Quantification of recruitment of the different markers for VDIMs was performed manually using maximum-intensity projections of Airyscan super-resolution images.

Time-lapse images. For fluorescence intensity measurements from time-lapse images, processed Airyscan images were analysed using ImageJ (Fiji) software. ROIs were selected around entire mitochondria from where the VDIM pinched off at each time frame, and mitotracker intensity was measured. For analysis of VDIMs, dextran-labelled lysosomes were used to select the region of interest and the mean fluorescence intensity for indicated channels within the ROI was measured over time.

3D reconstruction. Surface reconstruction of fluorescence images acquired from Airyscan images as described above was processed using Imaris Bitplane 9.5 software using the 'surface' feature and default parameters (Oxford Instruments)

Statistical analysis

Data shown are mean ± s.e.m. from independent biological replicates. No randomization or blinding was applied in this study and no statistical methods were used to predetermine sample sizes. As indicated, comparison between two groups was performed using unpaired two-tailed Student's t-test, and comparison between multiple groups was performed using one-way ANOVA with Tukey's multiple-comparison test with Prism software (GraphPad Software). P values calculated are indicated, the 95% confidence interval was used to determine statistical significance and $P < 0.05$ was considered statistically significant.

Material availability

The *Atg5*$^{-/-}$ and *Atg16L1*$^{-/-}$ MEFs and littermate WT controls were obtained under a material transfer agreement from T. Yoshimori (Osaka University), and *Trpml1*$^{-/-}$ and littermate WT MEFs were derived from mice obtained from S. Slaugenhaupt (Harvard Medical School) under a material transfer agreement. All requests for materials and reagents should be directed to the corresponding author N.L.J. (Nicola.jones@sickkids.ca).

Reporting summary

Further information on research design is available in the Nature Portfolio Reporting Summary linked to this article.

Data availability

All data supporting the conclusions of this study are available in the main text or Extended Data Figs. 1–10. Full versions of blots and gels are provided in Supplementary Figs. 1 and 2. Source data are provided with this paper.

51. Elia, N., Sougrat, R., Spurlin, T. A., Hurley, J. H. & Lippincott-Schwartz, J. Dynamics of endosomal sorting complex required for transport (ESCRT) machinery during cytokinesis and its role in abscission. *Proc Natl Acad. Sci. USA* **108**, 4846–4851 (2011).
52. Bagshaw, R. D., Callahan, J. W. & Mahuran, D. J. The Arf-family protein, Arl8b, is involved in the spatial distribution of lysosomes. *Biochem. Biophys. Res. Commun.* **344**, 1186–1191 (2006).
53. Cemma, M., Kim, P. K. & Brumell, J. H. The ubiquitin-binding adaptor proteins p62/SQSTM1 and NDP52 are recruited independently to bacteria-associated microdomains to target *Salmonella* to the autophagy pathway. *Autophagy* **7**, 341–345 (2011).
54. Boutry, M. & Kim, P. K. ORP1L mediated PI(4)P signaling at ER-lysosome-mitochondrion three-way contact contributes to mitochondrial division. *Nat. Commun.* **12**, 5354 (2021).
55. Law, K. B. et al. The peroxisomal AAA ATPase complex prevents pexophagy and development of peroxisome biogenesis disorders. *Autophagy* **13**, 868–884 (2017).
56. Sargent, G. et al. PEX2 is the E3 ubiquitin ligase required for pexophagy during starvation. *J. Cell Biol.* **214**, 677–690 (2016).
57. Wang, Y., Nartiss, Y., Steipe, B., McQuibban, G. A. & Kim, P. K. ROS-induced mitochondrial depolarization initiates PARK2/PARKIN-dependent mitochondrial degradation by autophagy. *Autophagy* **8**, 1462–1476 (2012).
58. Roy, M., Itoh, K., Iijima, M. & Sesaki, H. Parkin suppresses Drp1-independent mitochondrial division. *Biochem. Biophys. Res. Commun.* **475**, 283–288 (2016).
59. Kageyama, Y. et al. Parkin-independent mitophagy requires Drp1 and maintains the integrity of mammalian heart and brain. *EMBO J.* **33**, 2798–2813 (2014).
60. Fujita, N. et al. Recruitment of the autophagic machinery to endosomes during infection is mediated by ubiquitin. *J. Cell Biol.* **203**, 115–128 (2013).
61. Yan, B. R. et al. C5orf51 is a component of the MON1-CCZ1 complex and controls RAB7A localization and stability during mitophagy. *Autophagy* **18**, 829–840 (2022).
62. Durkin, M., Qian, X., Popescu, N. & Lowy, D. Isolation of mouse embryo fibroblasts. *Bio Protoc.* **3**, e908 (2013).
63. Paul-Gilloteaux, P. et al. eC-CLEM: flexible multidimensional registration software for correlative microscopies. *Nat. Methods* **14**, 102–103 (2017).

Acknowledgements This work was supported by grants from the Canadian Institute of Health Sciences to N.L.J. (CIHR operating grant nos. 142228 and 173335). A.P. was supported by the Restracomp Fellowship (Hospital for Sick Children). H.S. is supported by NIH grant no. R35GM144103. M.G.G. is supported by Cancer Research UK grant no. FC001092, UK Medical Research Council grant no. CC2081 and Wellcome Trust grant no. CC2081. C.B. was supported by European Respiratory Society–Marie Sklodowska-Curie grant no. 713406. We thank S. Slaugenhaupt (Harvard Medical School, USA) for TRPML1-deficient mice. We thank T. Yoshimori (Osaka University, Tokyo) for generously providing the *ATG14*$^{-/-}$ and *ATG16L1*$^{-/-}$ MEFs. We thank M. R. Terebiznik (University of Toronto at Scarborough, Toronto) for engaging discussions, and K. Lau and P. Paroutis at the imaging facility at the Hospital for Sick Children for assistance with image analysis.

Author contributions A.P. performed and analysed all light microscopy imaging studies and immunoblots. C.B. and A.F. performed and analysed electron microscopy and CLEM studies. X.G. generated the MCU-mCherry-GFP construct and contributed to the generation of *Trpml1*$^{-/-}$ MEFs. M.G.G. and N.L.J. contributed to project supervision. A.P., M.I.C., H.S., M.G.G. and N.L.J. designed the study. A.P. wrote the original draft. C.B., A.F., M.I.C., H.S., M.G.G. and N.L.J. contributed to manuscript writing and editing.

Competing interests The authors declare no competing interests.

Additional information

Supplementary information The online version contains supplementary material available at https://doi.org/10.1038/s41586-024-07835-w.

Correspondence and requests for materials should be addressed to Nicola L. Jones.

Peer review information *Nature* thanks the anonymous reviewers for their contribution to the peer review of this work. Peer reviewer reports are available.

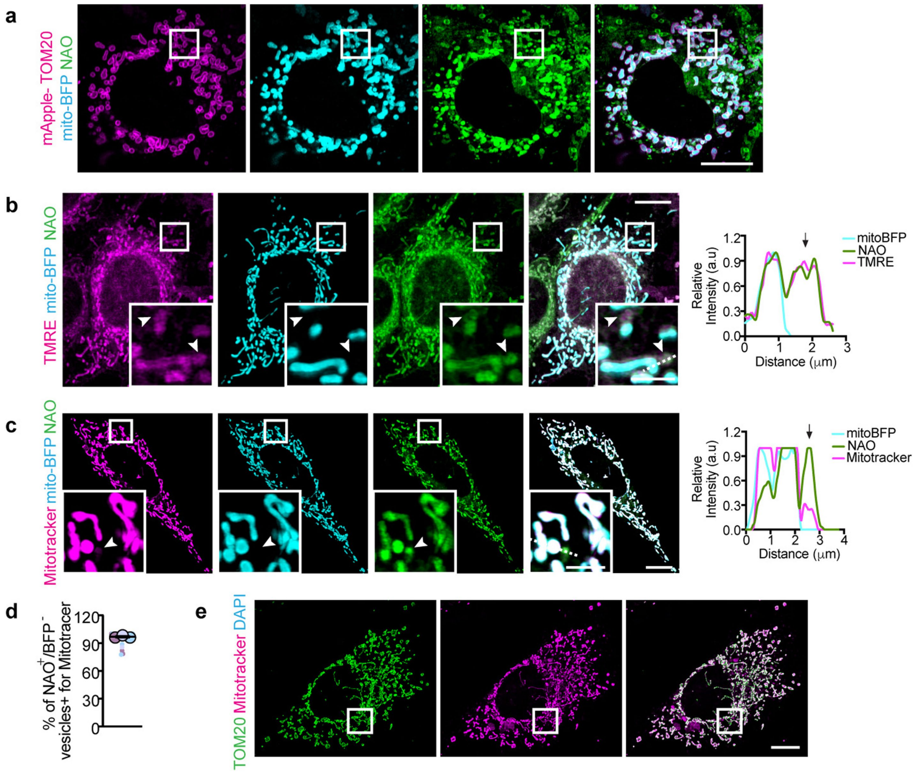

Extended Data Fig. 1 | Cytosolic IMM-derived vesicles lack matrix and OMM. a, TOM20 and NAO localization. Inner mitochondrial membranes were labeled with NAO (green) in cells expressing mito-BFP (cyan) and mApple-TOM20 (magenta). Higher magnifications of indicated regions are shown in Fig. 1a. **b**, Localization of TMRE (magenta), NAO (green) in cells expressing mito-BFP (cyan). Higher magnifications of indicated regions are shown. Arrowheads indicate mito-BFP$^-$/NAO$^+$/TMRE$^+$ vesicles. **Right**: Pixel intensity plots for dashed line. Arrow indicates the vesicle. **c**, NAO (green), mitotrackerCMX Ros (mitotracker) (magenta) localization in cell expressing mito-BFP (cyan). Higher magnifications of indicated regions are shown. Arrowheads indicate mito-BFP$^-$/NAO$^+$/mitotracker$^+$ vesicle. **Right**: Pixel intensity plots for dashed line. Arrow indicates the vesicle. **d**, Percentage of vesicles positive for IMM markers NAO and mitotracker, but negative for mito-BFP from experiments as in (**c**) (n = 365 vesicles, 30 cells, 3 experiments). Data shown are mean ± SEM shown as large circles and individual data points from corresponding experiments are shown in the same color (**e**) Representative images from at least three independent experiments showing mitotracker (magenta) and TOM20 (green) localization. Higher magnifications of indicated regions are shown in Fig. 1c. Scale bars: main panels 10 μm, magnified panels 3 μm.

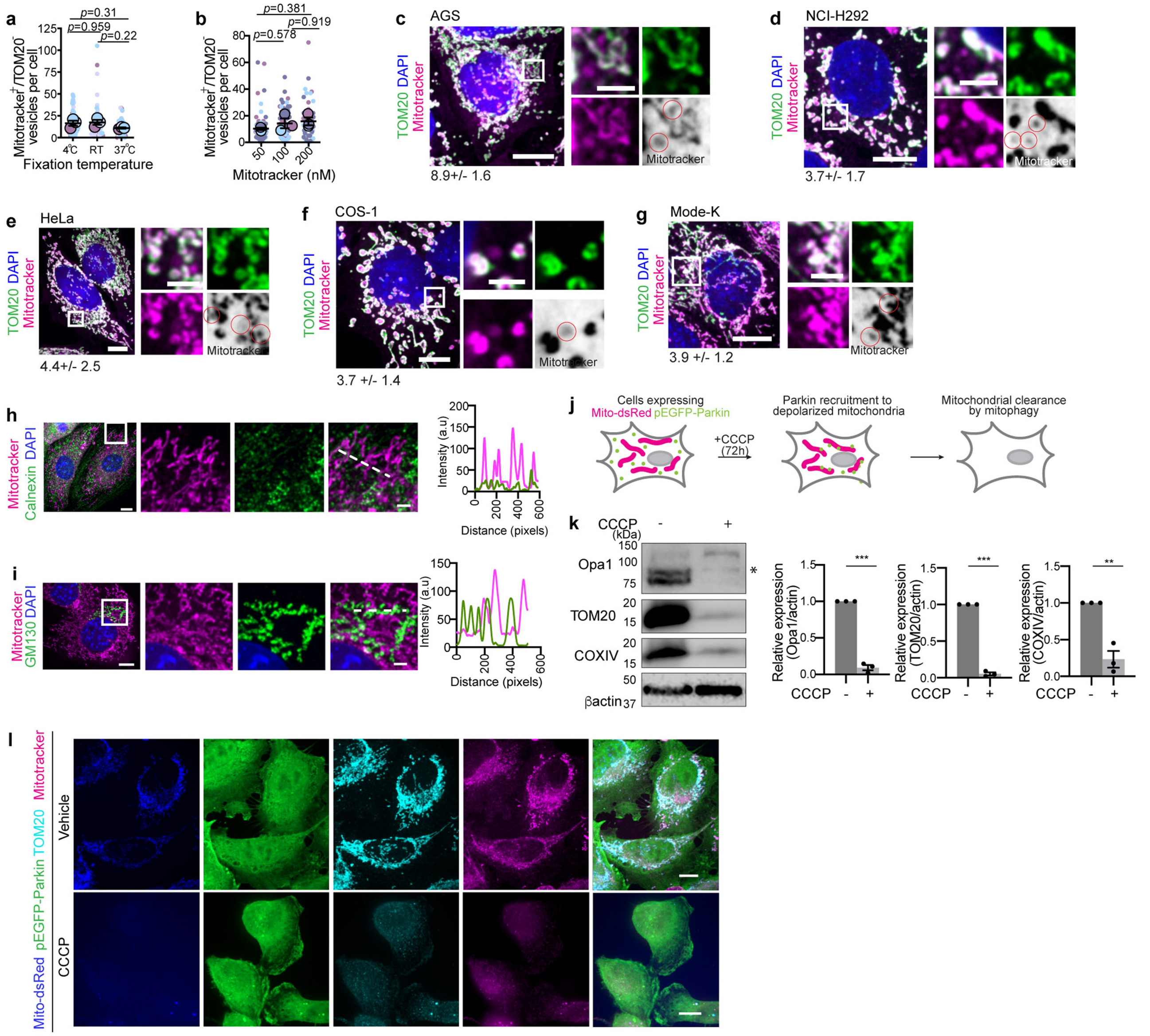

Extended Data Fig. 2 | Validating specificity of IMM in VDIMs. a, Effect of fixation conditions on mitotracker$^+$/TOM20$^-$ vesicles. Cells labeled with mitotracker (100 nM, 15 min, 37 °C) were either fixed for 15 min at room temperature (RT), 4 °C overnight or at 37 °C in pre-warmed 4% paraformaldehyde for 10 min (n = 60 cells, 3 experiments). **b**, Effect of mitotracker concentration on mitotracker$^+$/TOM20$^-$ vesicles. Cells were stained with indicated concentrations of mitotracker (n = 62 cells for 50 nM, 64 cells for 100 nM, 53 cells for 200 nM, 3 experiments). **c**-**g**, Mitotracker$^+$/TOM20$^-$ vesicles are cell-type independent. Spinning disc confocal images of mitotracker$^+$/TOM20$^-$ vesicles in (**c**) AGS (n = 4 experiments), (**d**) NCI-H292 (n = 4 experiments), (**e**) HeLa (n = 2 experiments), (**f**) COS-1 (n = 2 experiments), and (**g**) Mode-K (n = 3 experiments) cells. For all images, numbers at the bottom indicate the number of vesicles (mean ± SEM), and higher magnifications from indicated regions from main panels are shown to the right. Inverse color micrographs for mitotracker channel are shown. Red circles indicate the mitotracker$^+$/TOM20$^-$ vesicles. **h**,**i**, Mitotracker does not label membranes non-specifically. Spinning disc confocal images showing localization of mitotracker (magenta) and ER specific Calnexin (green) (**h**), or Golgi specific GM130 (green) (**i**). **Right**: Pixel intensity plot for dashed lines. **j**, Schematic illustrating the protocol for depleting mitochondria from HeLa cells stably expressing Mito-dsRed and pEGFP-Parkin. **k**, Western blot showing the depletion of mitochondrial proteins in cells from (**j**). **Right**: Protein expression relative to actin. **l**, Spinning disc confocal images showing lack of mitochondrial labeling by mitotracker (magenta) in HeLa cells expressing mito-dsRed (blue) and pEGFP-Parkin (green), labeled with anti-TOM20 antibodies (cyan) in an experiment as in (**j**). Data shown are mean ± SEM from three independent experiments. Statistical significance was calculated using One-way ANOVA followed by Tukey's multiple-comparison test in (**a**-**b**), and two-tailed Student's unpaired t-test in (**k**). *P* values calculated are shown. Gel source data for (**k**) are provided in Supplementary Fig. 1. Scale bars: main panels 10μm, magnified panels 3μm.

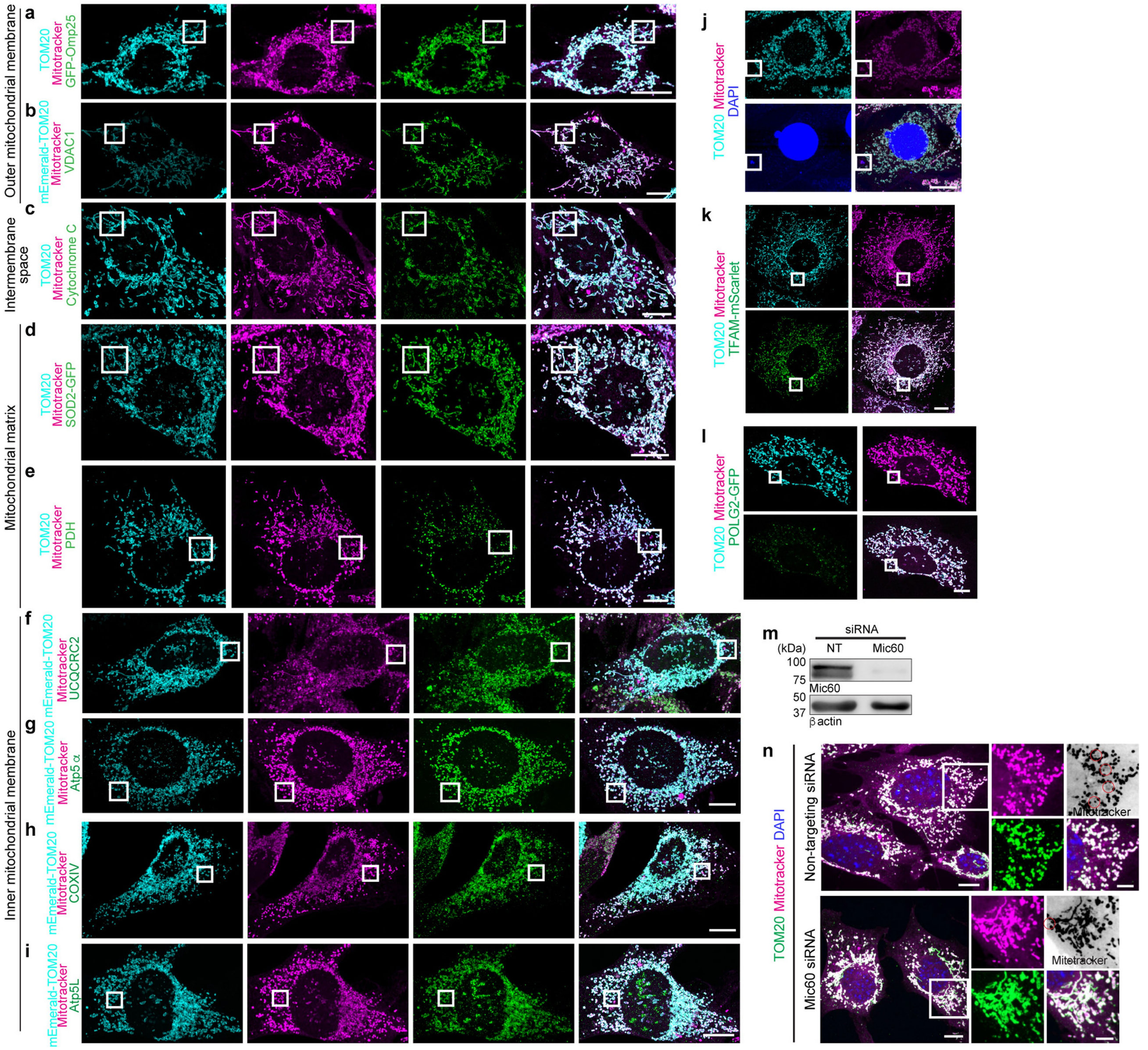

Extended Data Fig. 3 | VDIMs are derived from the IMM. a-**i**, Localization of mitotracker along with markers associated with different mitochondrial compartments. **a**,**b**, Representative images showing localization of mitotracker (magenta) and OMM localized (**a**) Omp25 (green) and TOM20 (cyan), or (**b**) VDAC1 (green) and mEmerald-TOM20 (cyan). Higher magnifications of the indicated regions are shown in Fig. 1g. **c**, Representative images showing localization of mitotracker (magenta) and mitochondrial intermembrane space-localized cytochrome C (green). OMM was labeled with anti-TOM20 antibodies (cyan). Higher magnifications of the indicated regions are shown in Fig. 1h. **d**,**e**, Representative images showing localization of mitotracker (magenta), TOM20 (cyan) and mitochondrial matrix-localized (**d**) SOD2 (green) and (**e**) PDH (green). Higher magnifications of the indicated regions are shown in Fig. 1i. **f**-**i**, Representative images showing localization of mitotracker (magenta) in cells expressing mEmerald-TOM20(cyan) and mitochondrial IMM-localized (**f**) UCQCRC2, (**g**) Atp5α, (**h**) COXIV and (**i**) Atp5L (green). Higher magnifications of the indicated regions are shown in Fig. 1j. (**j**) Representative images showing MEFs labeled with mitotracker (magenta), anti-TOM20 antibodies (cyan) and high concentration of DAPI (5 µg/ml). Higher magnifications of indicated regions are shown in Fig. 1m. **k**, Localization of TOM20 (cyan) and mitotracker (magenta) in cells expressing TFAM-mScarlet (green). Higher magnifications of indicated regions are shown in Fig. 1o. **l**, Localization of TOM20 (cyan) and mitotracker (magenta) in cells expressing POLG2-tGFP (green). Higher magnifications of indicated regions are shown in Fig. 1q. **m**, Representative western blot showing the efficiency of Mic60 knockdown. Cells were treated with indicated siRNA. **n**, VDIM formation in cells treated with indicated siRNA. Mitochondria were labeled with mitotracker (magenta) and anti-TOM20 antibodies (green). Representative confocal images from three independent experiments (**a**-**l**) and four independent experiments (**n**) are shown. Gel source data for (**m**) are provided in Supplementary Fig. 1. Scale bars: main panels 10 µm, magnified panels 3 µm. Red circles in the inverted mitotracker micrographs indicate the VDIMs.

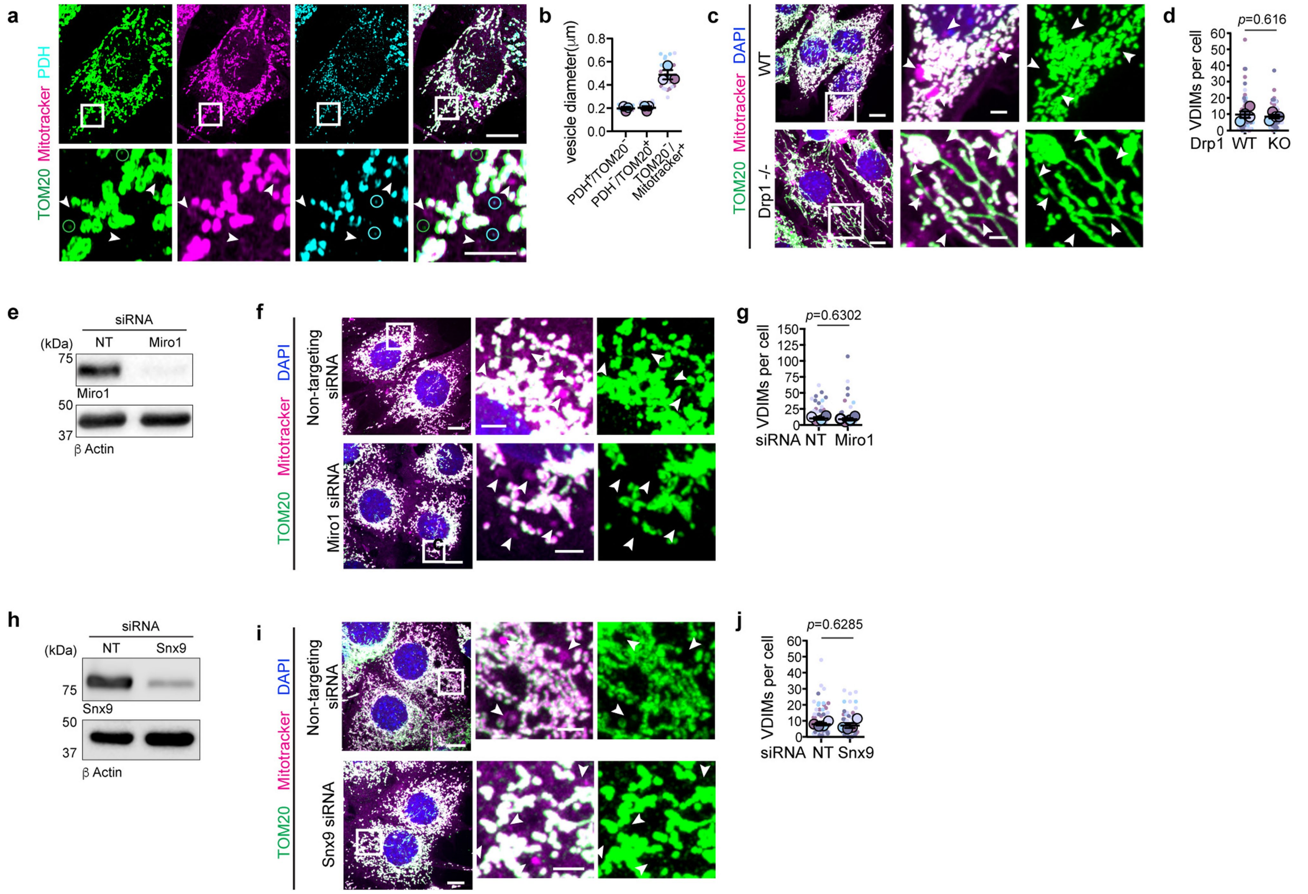

Extended Data Fig. 4 | VDIMs are distinct from MDVs and MDCs. a, VDIMs are larger than MDVs. Size difference between the Tom20 (green) or PDH (cyan) positive mitochondria derived vesicles (MDVs) (indicated by open circles), and mitotracker$^+$/TOM20$^-$ vesicles (arrowheads). **Bottom**: Higher magnifications of indicated regions. **b**, Size difference between the Tom20 (green) or PDH (cyan) positive mitochondria derived vesicles (MDVs) (indicated by open circles), and mitotracker$^+$/TOM20$^-$ vesicles (arrowheads) in experiments as in (**a**) (n = 562 vesicles, 30 cells, 3 experiments for PDH$^+$/TOM20$^-$ vesicles; n = 605 vesicles, 30 cells, 3 experiments for PDH$^-$/TOM20$^+$ vesicles; n = 436 vesicles, 30 cells, 3 experiments for mitotracker$^+$/TOM20$^-$ vesicles). **c**, Representative spinning disc confocal images showing VDIM formation in WT and Drp1$^{-/-}$ MEFs. Arrowheads indicate VDIMs. **d**, Number of VDIMs in WT and Drp1$^{-/-}$ (KO) MEFs in experiments as in (**c**) (n = 80 cells, 4 experiments). **e**, Representative western blot (n = 4 experiments) showing loss of Miro1 expression in cells treated with non-targeting (NT) siRNA or siRNA against Miro1. **f**, Representative spinning disc confocal images showing VDIM formation in cells treated with NT or Miro1 siRNA an experiment as in (**e**). Arrowheads indicate VDIMs. **g**, Number VDIMs in cells treated with non-targeting (NT) or Miro1 siRNA in experiments as in (**f**) (n = 90 cells, 4 experiments). **h**, Representative western blot (n = 4 experiments) showing loss of sorting nexin 9 (Snx9) expression in cells treated with non-targeting (NT) siRNA or siRNA against Snx9. **i**, Representative spinning disc confocal images showing VDIM formation in cells in experiments as in (**h**). **j**, Number of VDIMs in cells treated with non-targeting (NT) or syntaxin 9 (snx9) siRNA in experiments as in (**i**) (n = 90 cells, 4 experiments). Data shown are mean ± SEM from three independent experiments. Statistical significance was calculated using two-tailed Student's unpaired t-test. Gel source data for (**e**,**h**) are provided in Supplementary Fig. 1. Scale bars: main panels 10 µm, magnified panels 3 µm.

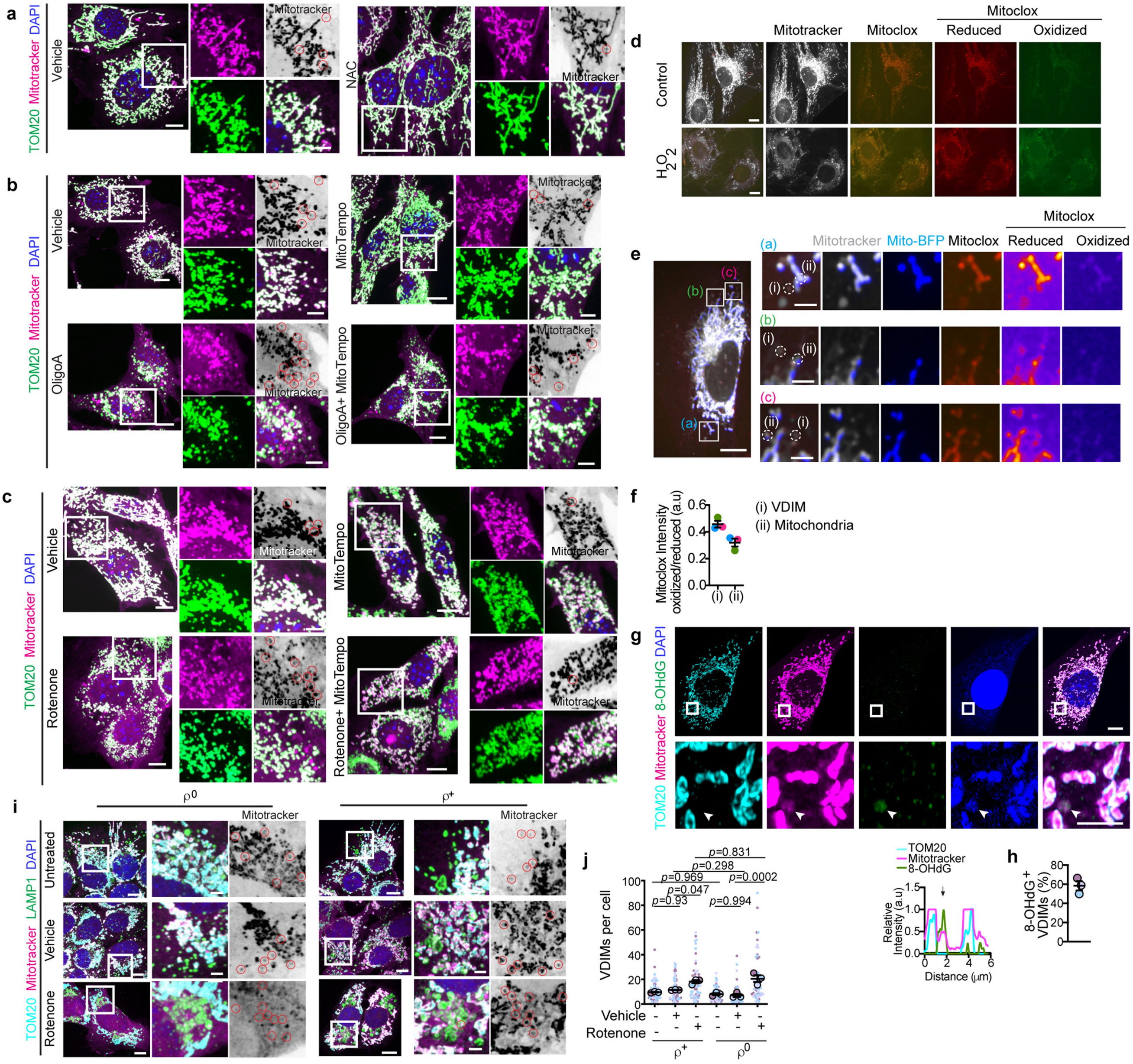

Extended Data Fig. 5 | VDIM formation for intramitochondrial QC. a, VDIM formation is inhibited by quenching ROS. Representative spinning disc confocal micrographs showing the effect of NAC on VDIM formation. Red circles in the inverted color mitotracker micrographs indicate VDIMs. **b**,**c**, Representative confocal micrographs showing the effect of inducing oxidative stress on VDIM formation. Cells were treated with (**b**) oligomycinA, mitoTempo or oligomycinA+ mitoTempo, or (**c**) with rotenone, mitoTempo or rotenone+mitoTempo. Mitochondria were labeled with mitotracker (magenta) and anti-TOM20 antibodies (green). Red circles in the inverted color mitotracker micrographs indicate VDIMs. **d**, Representative images showing oxidation of MitoCLox in cells treated with H_2O_2. **e**, Representative images showing oxidized MitoCLox in VDIMs (n = 3 experiments). **Right**: Higher magnification of indicated regions. **f**, Ratio of oxidized/total MitoCLox in indicated regions from (**e**). **g**, Localization of 8-OHdG (green) with VDIMs (arrowheads). **Bottom:** Pixel intensity plot for dashed line. Arrow indicates the vesicle. **h**, Percentage of VDIMs positive for 8-OHdG in experiments as in (**g**). (n = 272 vesicles, 32 cells, 3 experiments). **i**, Representative spinning disc confocal images showing localization of TOM20 (cyan), mitotracker (magenta) and LAMP1 (green) in 143bρ^0 and 143bρ$^+$ cells. Cells were left untreated or treated with vehicle or Rotenone. Higher magnifications of indicated regions are shown to the right. **j**, Quantification of VDIM formation in 143b cells lacking mitochondrial DNA (ρ0) along with controls (ρ+) (143bρ^0 n = 70 cells for untreated, 63 cells for vehicle, 60 cells for rotenone and 143bρ$^+$ n = 66 cells for untreated, 61 cells for vehicle, 60 cells for rotenone, 3 experiments). Data shown are mean ± SEM shown as large circles and individual data points from corresponding experiments shown in the same colors. Statistical significance was calculated using One-way ANOVA followed by Tukey's multiple-comparison test. *P* values calculated are indicated. Scale bars: main panels 10 μm, magnified panels 3 μm.

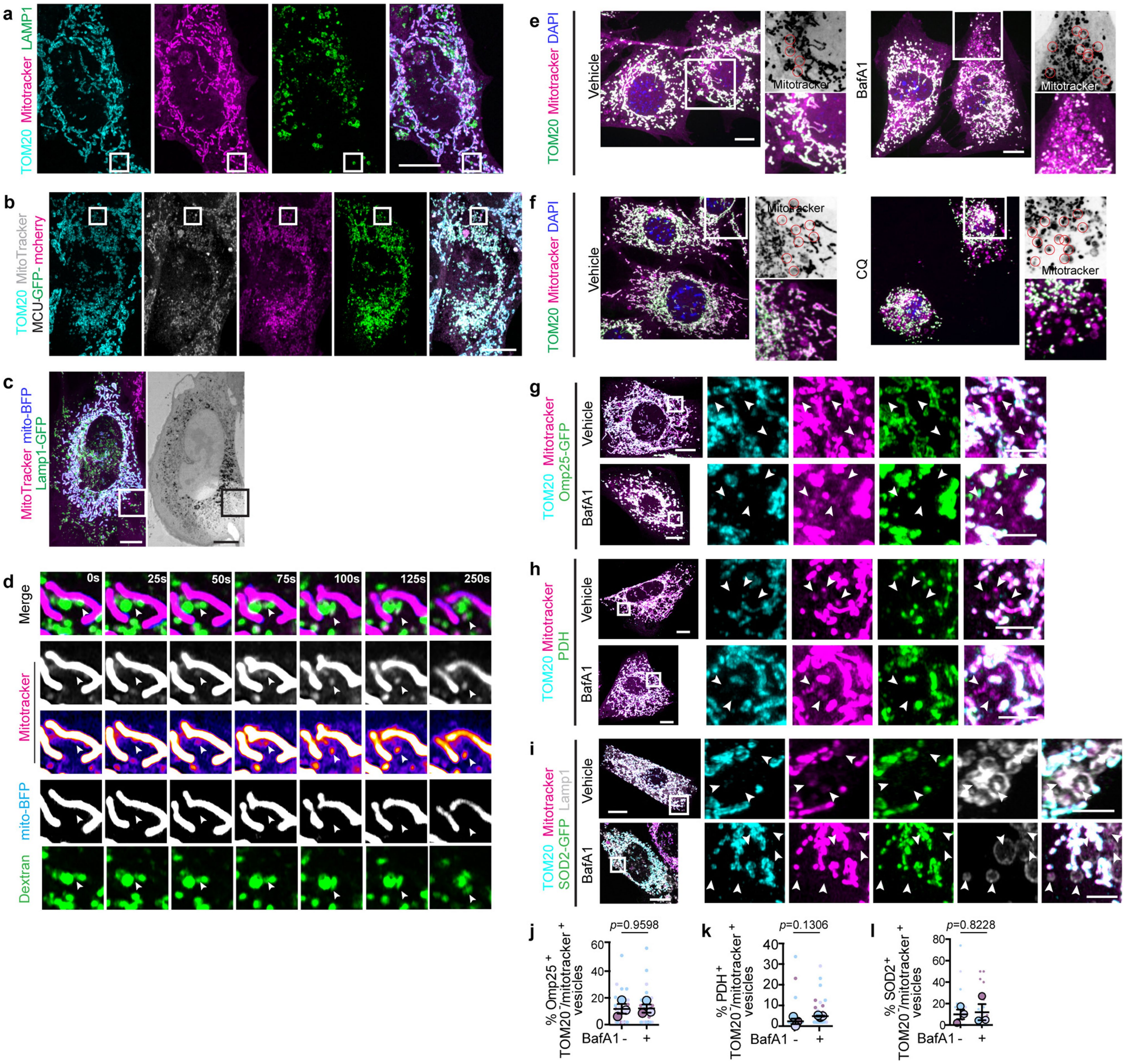

Extended Data Fig. 6 | VDIMs are delivered to lysosomes for degradation. **a**, Mitotracker (magenta), TOM20 (cyan) and LAMP1 (green) localization. Higher magnifications of indicated regions are shown in Fig. 3a. **b**, Localization of mitotracker (grey), TOM20 (cyan) and MCU-GFP-mCherry. Higher magnifications of indicated regions are shown in Fig. 3d. **c**, **Left:** Fluorescence, and **Right:** EM image of cell used for CLEM. Higher magnification of indicated region is shown in Fig. 3f. **d**, Live-cell imaging showing mito-BFP$^-$/mitotracker$^+$ (magenta) vesicles being delivered to lysosomes labeled with dextran (green). Arrowheads indicate the VDIM pinching from the mitochondria and sorted to the lysosome. Images were acquired every 5 s. **e**-**l**, VDIMs are not partially degraded mitochondria. **e**, Representative spinning disc confocal micrographs showing the effect of bafilomycin (BafA1) on VDIM formation. **Right**: Higher magnifications of indicated regions. Red circles in inverted micrograph for mitotracker indicate the VDIMs. **f**, Representative spinning disc confocal micrographs showing the effect of chloroquine (CQ) on VDIM formation. **Right**: Higher magnification of indicated regions. Red circles in inverted micrograph for mitotracker indicate the VDIMs. **g**, Localization of mitotracker (magenta), TOM20 (cyan) in cells expressing Omp25-GFP (green), treated with vehicle (-) or BafA1. Arrowheads indicate the VDIMs. (**h**) Localization of mitotracker (magenta), TOM20 (cyan) and PDH (green) in cells treated with vehicle (-) or BafA1. Arrowheads indicate the VDIMs. **i**, Localization of mitotracker (magenta), TOM20 (cyan) in cells expressing SOD2-GFP (green), treated with vehicle (-) or BafA1. Arrowheads indicate the VDIMs. **j**, Percentage of mitotracker$^+$/TOM20$^-$ VDIMs positive for Omp25 in cells treated with BafA1 compared to vehicle treated cells from experiments as in (**g**) (n = 270 vesicles for vehicle, 503 vesicles for BafA1, 30 cells, 3 experiments). **k**, Percentage of mitotracker$^+$/TOM20$^-$ VDIMs positive for PDH in cells treated with BafA1 compared to vehicle treated cells from experiments as in (**h**) (n = 270 vesicles for vehicle, 503 vesicles for BafA1, 30 cells, 3 experiments). **l**, Percentage of mitotracker$^+$/TOM20$^-$ VDIMs positive for SOD2 in cells treated with BafA1 compared to vehicle treated cells from experiments as in (**i**) (n = 369 vesicles for vehicle, 500 vesicles for BafA1, 30 cells, 3 experiments). (**j**-**l**) Mean ± SEM are shown as large circles and individual data points from corresponding experiments are shown in the same colors. Statistical analysis was performed using two-tailed Student's unpaired t-test. *P* values are indicated. Scale bars: main panels 10 µm, magnified panels 3 µm.

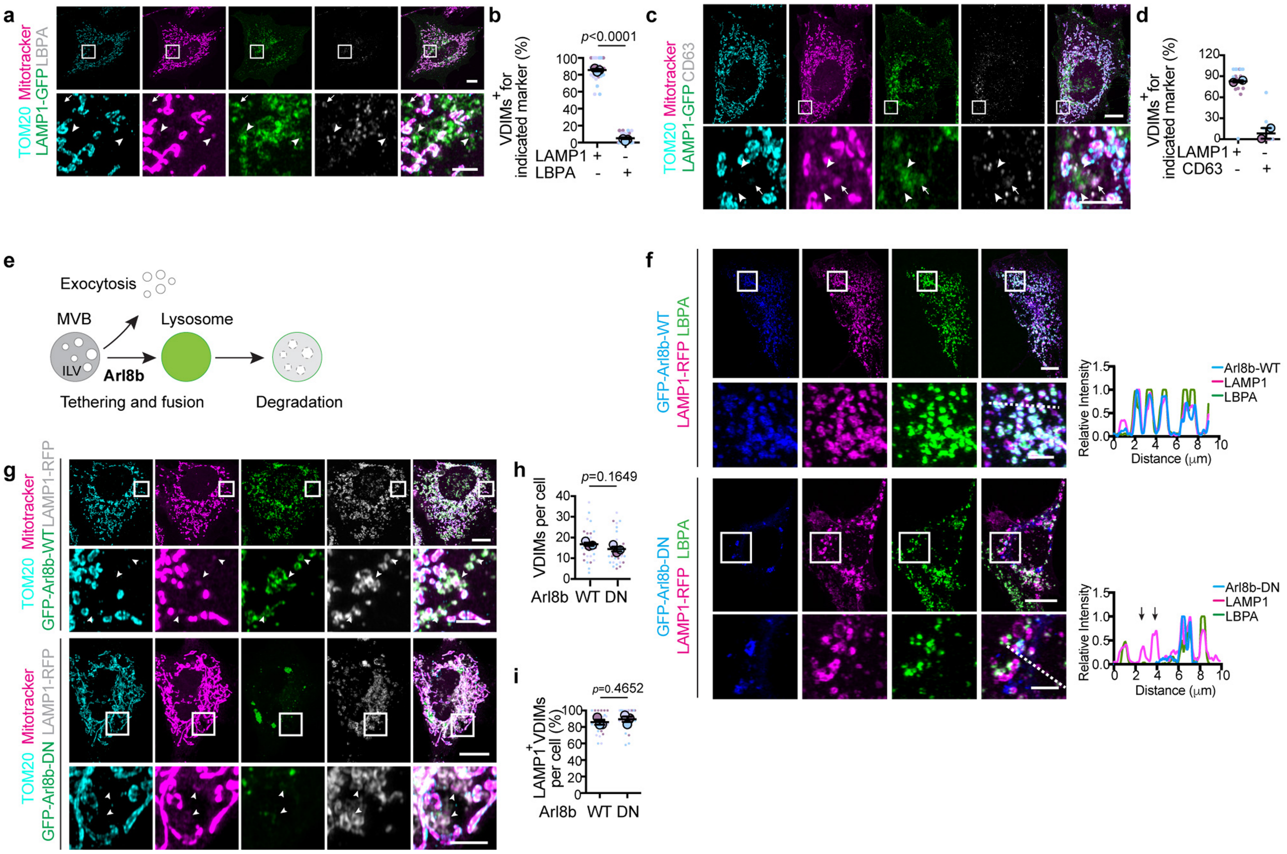

Extended Data Fig. 7 | VDIMs are not multivesicular bodies (MVB). **a**, Representative images showing mitotracker (magenta), TOM20 (cyan), LBPA (grey) in cells expressing LAMP1-GFP (green). **Bottom**: Higher magnification of indicated regions. Arrowheads indicate VDIMs lacking LBPA. Arrow indicates VDIM positive for LBPA. **b**, Number of VDIMs positive for LAMP1 or LBPA from experiments as in (**a**) (n = 243 vesicles, 30 cells, 3 experiments). **c**, Representative images showing mitotracker (magenta), TOM20 (cyan), CD63 (grey) in cells expressing LAMP1-GFP (green). **Bottom**: Higher magnification of indicated regions. Arrowheads indicate VDIMs lacking CD63. Arrow indicates VDIM positive for CD63. **d**, Number of VDIMs positive for LAMP1 or CD63 from experiments as in (**c**) (n = 167 vesicles, 17 cells, 2 experiments). **e**, Schematic illustrating lysosome and MVB fusion regulated by Arl8b GTPase. **f**, Localization of Lamp1 (magenta) and LBPA (green) in cells expressing GFP-Arl8b-WT (blue) or GFP-Arl8b-DN (blue). **Right**: Pixel intensity plots for dashed line. Arrows indicate LBPA negative lysosomes in cells expressing GFP-Arl8b-DN. **g**, VDIM formation in cells expressing GFP-Arl8b-WT (green) or GFP-Arl8b-DN (green). Higher magnification of indicated regions are shown where arrowheads indicate the VDIM. **h**, Number of VDIMs in cells expressing Arl8b-WT or Arl8b-DN in experiments as in (g) (n = 30 cells, 3 experiments). **i**, Number of LAMP1 positive VDIMs in cells expressing Arl8b-WT or Arl8b-DN in experiments as in (**g**) (n = 30 cells, 3 experiments). Data shown are mean ± SEM. Statistical significance was calculated using two-tailed Student's unpaired t-test. *P* values calculated are indicated. Scale bars: main panels 10 µm, magnified panels 3 µm.

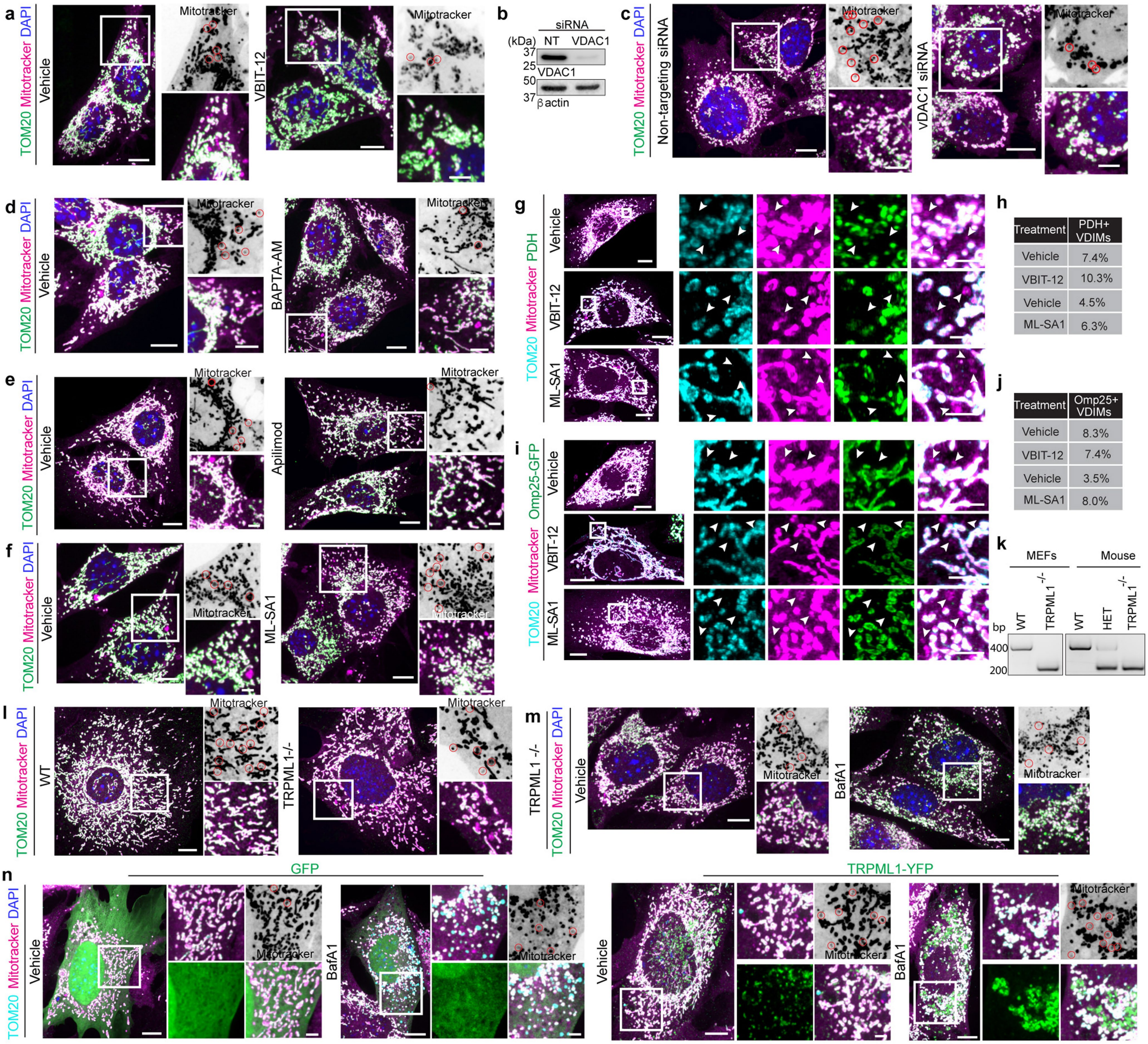

Treatment	PDH+ VDIMs
Vehicle	7.4%
VBIT-12	10.3%
Vehicle	4.5%
ML-SA1	6.3%

Treatment	Omp25+ VDIMs
Vehicle	8.3%
VBIT-12	7.4%
Vehicle	3.5%
ML-SA1	8.0%

Extended Data Fig. 8 | VDAC1 and TRPML1 mediate VDIM formation. **a**, VDIM formation in cells treated with vehicle or VBIT-12. **b**, Representative western blot showing the efficiency of VDAC1 knockdown (n = 4 experiments). **c**, VDIM formation in cells treated with indicated siRNA. **d**, VDIM formation in cells treated with BAPTA-AM. **e**, VDIM formation in cells treated with apilimod. **f**, VDIM formation in cells treated with ML-SA1. **g**, Mitotracker (magenta), TOM20 (cyan) and PDH (green) localization in cells treated with VBIT-12 or ML-SA1. Arrowheads indicate the VDIMs. **h**, Percentage of mitotracker$^+$/TOM20$^-$ VDIMs positive for PDH in experiments as in (**g**) (n = 293 vesicles for vehicle, 535 vesicles for ML-SA1, 30 cells, 3 experiments for ML-SA1; n = 342 vesicles for vehicle, 302 vesicles for VBIT-12, 30 cells, 3 experiments). **i**, Mitotracker (magenta), TOM20 (cyan) in cells expressing Omp25-GFP (green) treated with VBIT-12 or ML-SA1. Arrowheads indicate the VDIMs. **j**, Percentage of mitotracker$^+$/TOM20$^-$ VDIMs positive for Omp25 in experiments as in (**i**). **k**, Validation of gene knockout in TRPML1$^{-/-}$ MEFs. MLIV gene was amplified from WT and TRPML1$^{-/-}$ MEFs and from DNA extracted from ear-notches of WT, KO and heterozygous (het) mice (n = 1). **l**, Representative confocal micrographs showing VDIM formation in WT and TRPML1$^{-/-}$ MEFs. **m**, VDIM formation in TRPML1$^{-/-}$ MEFs treated with BafA1. **n**, Effect of TRPML1 re-expression on VDIM formation in TRPML1$^{-/-}$ MEFs. TRPML1$^{-/-}$ cells transiently transfected with GFP or TRPML1-YFP were treated with vehicle or BafA1. Data shown are means from 3 experiments. Representative spinning disc confocal micrographs are shown in (**a**, **c**-**f**, **l**-**n**). For all fluorescence images, higher magnifications of indicated regions are shown to the right. Red circles on the inverted fluorescence micrographs for the mitotracker channel indicate the VDIMs. Gel source data for (**b**) are provided in Supplementary Fig. 2. Scale bars: main panels 10 μm, magnified panels 3 μm.

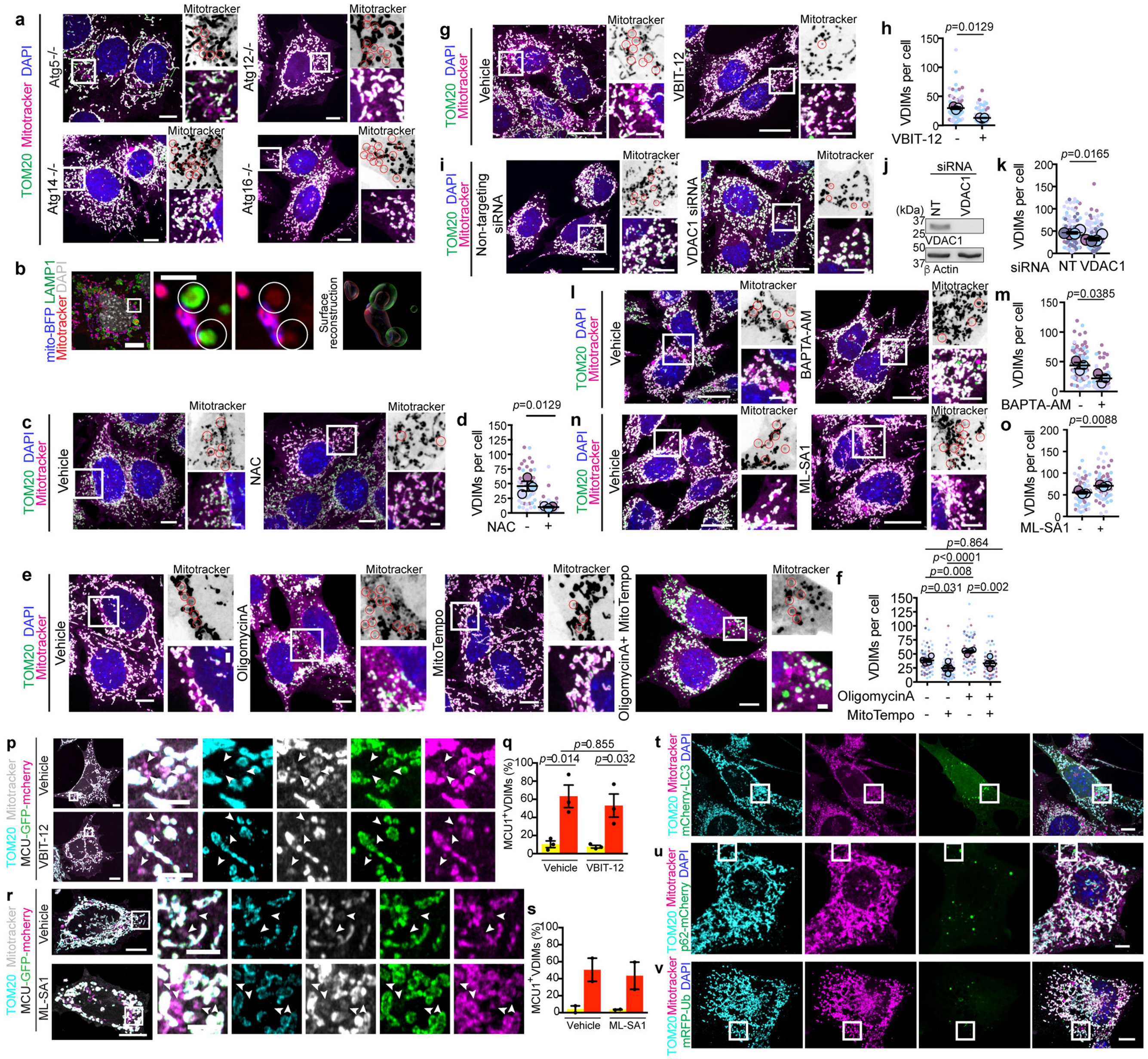

Extended Data Fig. 9 | VDIMs form independently of macroautophagy. **a**, VDIM formation in MEFs lacking Atg5, Atg12, Atg14 and Atg16. **Right**: Higher magnification of indicated regions. **b**, VDIM formation in Atg5−/− MEFs. Representative confocal micrographs showing VDIM pinching off and being directly sorted into a lysosome. **Right:** 3D- reconstruction of indicated region. **c**, Effect of scavenging ROS on VDIM formation. Cells were treated with vehicle (−) or NAC (+). **d**, Number of VDIMs in cells in experiments as in (**c**) (n = 63 cells, 3 experiments). **e**, Effect of oxidative stress on VDIM formation. Cells were treated with vehicle, oligomycinA, mitoTempo or oligomycinA and mitoTempo together. **f**, Number of VDIMs in cells in experiments as in (e) (n = 75 cells for vehicle, 64 cells for oligomycinA, 73 cells for mitoTempo, 66 for oligomycinA+ mitoTempo, 4 experiments). **g**, Effect of VDAC inhibition on VDIM formation. **h**, Number of VDIMs in cells treated with VBIT-12 in experiments as in (**g**) (n = 75 cells, 3 experiments). **i**, Representative images showing VDIM formation in cells treated with indicated siRNA. **j**, Representative western blot showing the efficiency of VDAC1 knockdown (n = 4 experiments). **k**, Number of VDIMs in VDAC1 depleted cells in experiments as in (**i**) (n = 136 cell for NT, 127 for VDAC siRNA, 4 experiments). **l**, Representative images showing the effect of BAPTA-AM on VDIM formation. **m**, Number of VDIMs in cells treated with BAPTA-AM in experiments as in (**l**) (n = 87 cells for vehicle, 67 cells for BAPTA-AM, 3 experiments). **n**, Representative images showing VDIM formation in cells treated with ML-SA1. **o**, Number of VDIMs in cells treated with ML-SA1 in experiments as in (**n**) (n = 66 cells for vehicle, 69 cells for ML-SA1, 3 experiments). **p**, Effect of VDAC1 inhibition on MCU-GFP-mCherry positive VDIMs. Cells expressing MCU-GFP-mCherry were treated with VBIT-12. **q**, Number of VDIMs positive for GFP+mCherry (yellow) and mCherry (red), indicating lysosomal quenching of GFP from experiments as in (**p**) (n = 412 vesicles for vehicle, 336 vesicles for VBIT-12, 30 cells, 3 experiments). **r**, Effect of TRPML1 activation by ML-SA1 on MCU-GFP-mCherry positive VDIMs. **s**, Number of VDIMs positive for GFP+mCherry (yellow) and mCherry (red), indicating lysosomal quenching of GFP from experiments as in (**r**) (n = 229 vesicles for vehicle, 194 vesicles for ML-SA1, 20 cells, 2 experiments). **t**-**v**, Localization of TOM20 (cyan) and mitotracker (magenta) with indicated autophagy markers. Cells were transfected with (**t**) mCherry-LC3 (green), (**u**) p62-mCherry (green), (**v**) mRFP-Ub (green). Higher magnifications of indicated regions are shown in Fig. 5e. Representative spinning disc confocal micrographs are shown in (**a**, **c**, **e**, **g**, **i**, **l**, **n**, **p**, **r**) where higher magnification of indicated regions are shown to the right. Red circles in inverted micrograph for mitotracker indicate the VDIMs. Data shown are mean ± SEM shown as large circles and individual data points from corresponding experiments shown in the same colors. Statistical significance was calculated using two-tailed Student's unpaired t-test in (**d**, **h**, **k**, **m**, **o**), and One-way ANOVA followed by Tukey's multiple-comparison test in (**f**, **q**, **s**). *P* values calculated are indicated. Gel source data for (**j**) are provided in Supplementary Fig. 1. Scale bars: main panels 10 μm, magnified panels 3 μm.

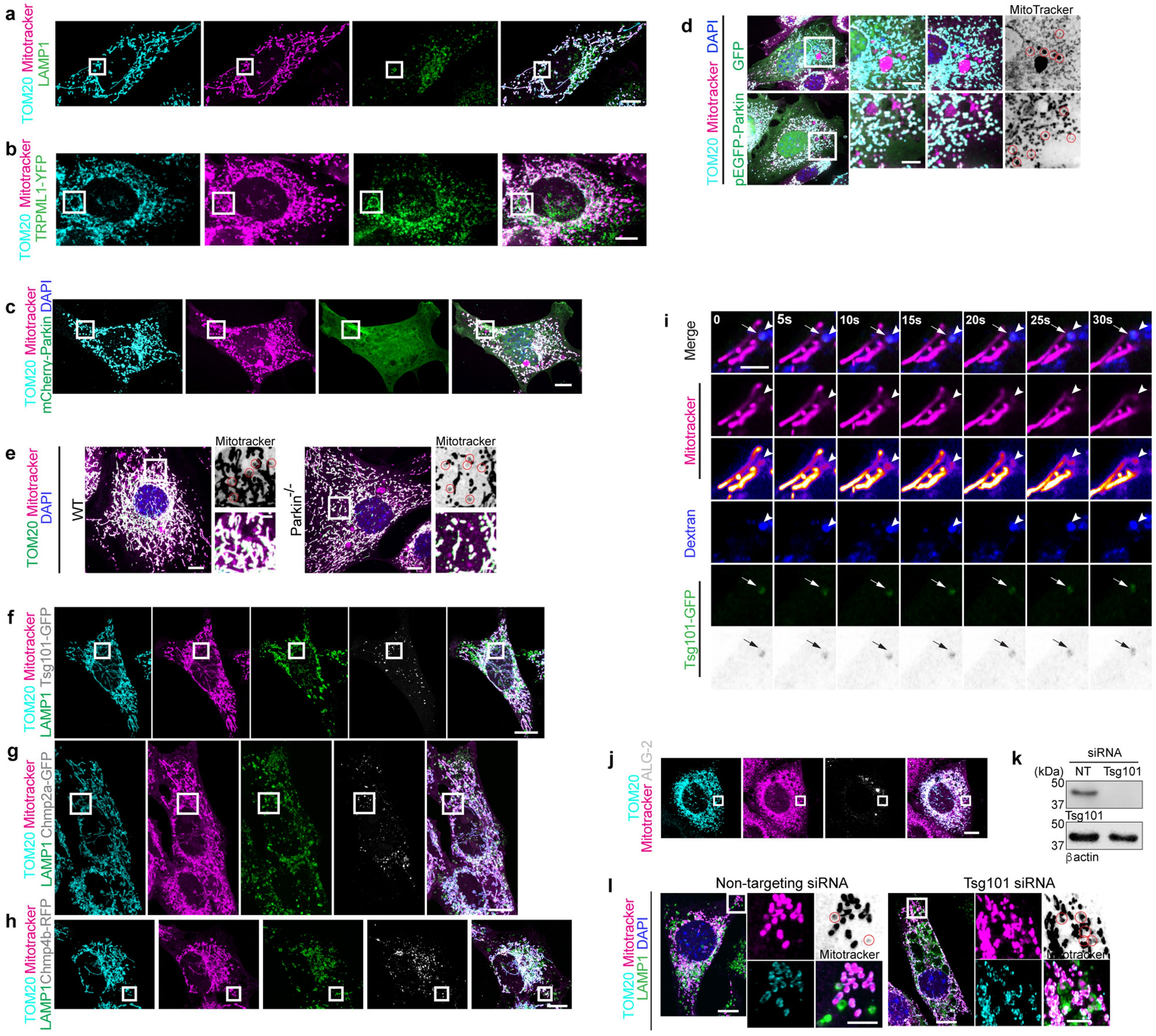

Extended Data Fig. 10 | VDIMs form by ESCRT-mediated, microautophagy-like process. a, Representative images showing TOM20 (cyan), mitotracker (magenta) and LAMP1 (green). Higher magnifications of indicated regions are shown in Fig. 5g. **b**, Representative images showing localization of TOM20 (cyan), mitotracker (magenta) and TRPML1 (green). Cells were transiently transfected with TRPML1-YFP. Higher magnifications of indicated regions are shown in Fig. 5h. **c**, Localization of TOM20 (cyan) and mitotracker (magenta) in cells expressing mCherry-Parkin. Higher magnification of indicated region is shown in Fig. 5i. **d**, Effect of Parkin overexpression on VDIM formation. Cells were transiently transfected with (top) GFP or (bottom) pEGFP-Parkin. Red circles in inverted micrographs for mitotracker indicate VDIMs. **e**, Representative images showing VDIM formation in Parkin-/- MEFs compared to WT controls. Circles in the inverted mitotracker micrograph indicate the VDIMs. **f-h**, Representative images showing localization of TOM20 (cyan), mitotracker (magenta) and LAMP1 (green) in cells transiently transfected with (**f**) Tsg101-GFP (grey), (**g**) Chmp2a-GFP (grey) or (**h**) Chmp4b-RFP (grey). Higher magnifications of indicated regions are shown in Fig. 6a–c. **i**, Live-cell imaging sequence showing recruitment of Tsg101 (green) at sites of VDIM scission. Images were acquired every 5 s. Arrowheads indicate the VDIMs and arrows indicate the Tsg101 puncta. **j**, Representative images showing mitotracker (magenta), TOM20 (cyan) and ALG-2 (grey). Higher magnifications of the indicated regions are shown in Fig. 6g. **k**, Representative western blot showing the efficiency of Tsg101 depletion compared to non-targeting (NT) controls. **l**, Representative images showing VDIM formation in cells treated with Tsg101 siRNA compared to NT controls. **Right**: Higher magnification of indicated regions. Red circles in inverted micrograph for mitotracker indicate the VDIMs. All data shown are representative from three independent experiments. **d**,**e**, Representative spinning disc confocal images are shown. Gel source data for (**k**) are provided in Supplementary Fig. 1. Scale bars: main panels 10 µm, magnified panels 3 µm.

nature portfolio

Corresponding author(s): Nicola Jones

Last updated by author(s): Jul 12, 2024

Reporting Summary

Nature Portfolio wishes to improve the reproducibility of the work that we publish. This form provides structure for consistency and transparency in reporting. For further information on Nature Portfolio policies, see our Editorial Policies and the Editorial Policy Checklist.

Statistics

For all statistical analyses, confirm that the following items are present in the figure legend, table legend, main text, or Methods section.

n/a	Confirmed	
☐	☒	The exact sample size (*n*) for each experimental group/condition, given as a discrete number and unit of measurement
☐	☒	A statement on whether measurements were taken from distinct samples or whether the same sample was measured repeatedly
☐	☒	The statistical test(s) used AND whether they are one- or two-sided *Only common tests should be described solely by name; describe more complex techniques in the Methods section.*
☒	☐	A description of all covariates tested
☐	☒	A description of any assumptions or corrections, such as tests of normality and adjustment for multiple comparisons
☐	☒	A full description of the statistical parameters including central tendency (e.g. means) or other basic estimates (e.g. regression coefficient) AND variation (e.g. standard deviation) or associated estimates of uncertainty (e.g. confidence intervals)
☐	☒	For null hypothesis testing, the test statistic (e.g. *F*, *t*, *r*) with confidence intervals, effect sizes, degrees of freedom and *P* value noted *Give P values as exact values whenever suitable.*
☒	☐	For Bayesian analysis, information on the choice of priors and Markov chain Monte Carlo settings
☒	☐	For hierarchical and complex designs, identification of the appropriate level for tests and full reporting of outcomes
☒	☐	Estimates of effect sizes (e.g. Cohen's *d*, Pearson's *r*), indicating how they were calculated

Our web collection on statistics for biologists contains articles on many of the points above.

Software and code

Policy information about availability of computer code

Data collection	Confocal images were acquired using Ziess LSM880 Airyscan microscope or Quorum Spinning disc confocal microscope with built in software, Zen Black with Airyscan super resolution module (v2.3 SP1, Zeiss) and Volocity (v6.3, Perkin Elmer), respectively. Western Blot membranes were obtained using an Odyssey FC instrument with Image Studio Software (LI-COR, v5.2.5).
Data analysis	Fixed and live-cell images were processed in Fiji (v1.0), 3D reconstructions of fluorescence images was performed in Imaris Bitplane (v9.5 , Oxford Instruments) using the default settings. Quantifications of number of VDIMs were performed on maximum intensity projections of images acquired using a Spinning disc confocal microscope, using Image J (Fiji, v1.0). Quantifications of recruitment of the different markers to VDIMs were performed manually using Fiji (v1.0) using maximum intensity projections of Airyscan superresolution images. Confocal images were aligned to EM micrographs with Icy software (v2.0.3.0,Institut Pasteur, France), using the ec-CLEM plugin (v1.0.1.5). Statistical significance was determined using Unpaired, two-tailed t-tests or One Way ANOVA as indicated using Graph pad prism (v6.0) and graphs were generated using Graph pad prism (v6.0). Western blot data was quantified using Image Studio (v5.2.5, LI-COR)

For manuscripts utilizing custom algorithms or software that are central to the research but not yet described in published literature, software must be made available to editors and reviewers. We strongly encourage code deposition in a community repository (e.g. GitHub). See the Nature Portfolio guidelines for submitting code & software for further information.

Data

Policy information about availability of data

All manuscripts must include a data availability statement. This statement should provide the following information, where applicable:

- Accession codes, unique identifiers, or web links for publicly available datasets
- A description of any restrictions on data availability
- For clinical datasets or third party data, please ensure that the statement adheres to our policy

All data supporting the conclusions of this study are available in the main text or extended figures. Source data for all the graphs are provided as separate excel files. Full versions of blots and gel are provided in Supplementary Figures.1-2.

Research involving human participants, their data, or biological material

Policy information about studies with human participants or human data. See also policy information about sex, gender (identity/presentation), and sexual orientation and race, ethnicity and racism.

Reporting on sex and gender	NA
Reporting on race, ethnicity, or other socially relevant groupings	NA
Population characteristics	NA
Recruitment	NA
Ethics oversight	NA

Note that full information on the approval of the study protocol must also be provided in the manuscript.

Field-specific reporting

Please select the one below that is the best fit for your research. If you are not sure, read the appropriate sections before making your selection.

☒ Life sciences ☐ Behavioural & social sciences ☐ Ecological, evolutionary & environmental sciences

For a reference copy of the document with all sections, see nature.com/documents/nr-reporting-summary-flat.pdf

Life sciences study design

All studies must disclose on these points even when the disclosure is negative.

Sample size	No statistical method was used to predetermine sample size. In order to ensure reproducibility and statistical significance, sample sizes were based on previously published studies assessing similar events (PMID: 27458136, PMID: 35025629). At least three biological replicates were used to test for statistical significance. The exact number of events analysed for each experiment are indicated in the Figure legend or Methods section
Data exclusions	No data were excluded from analysis
Replication	All experiments, with the exception of the correlative light and electron microscopy experiments (which were performed once) were performed with at least three independent repeats as detailed in the figure legends. All attempts at replication were successful
Randomization	For all analyses and quantifications, cells were randomly selected. To avoid bias, same software with identical settings between conditions was used for quantifications. The experimental setup included clearly defined conditions
Blinding	No blinding was performed for this study. Blinding was not necessary as quantifications were performed using software with identical settings

Reporting for specific materials, systems and methods

We require information from authors about some types of materials, experimental systems and methods used in many studies. Here, indicate whether each material, system or method listed is relevant to your study. If you are not sure if a list item applies to your research, read the appropriate section before selecting a response.

Materials & experimental systems

n/a	Involved in the study
☐	☒ Antibodies
☐	☒ Eukaryotic cell lines
☒	☐ Palaeontology and archaeology
☒	☐ Animals and other organisms
☒	☐ Clinical data
☒	☐ Dual use research of concern
☒	☐ Plants

Methods

n/a	Involved in the study
☒	☐ ChIP-seq
☒	☐ Flow cytometry
☒	☐ MRI-based neuroimaging

Antibodies

Antibodies used	The following primary antibodies were used for immunofluorescence analysis: anti-TOM20 (Proteintech, #11802-1-AP, 1:500), anti-cytochrome C (Abcam, #ab110325, 1:500), anti-PDH (Abcam, #ab110333, 1:500), anti-Atp5L (Proteintech, #16483, 1:500), anti-Atp5 (Abcam, #ab14748, 1:500), anti-VDAC1 (Abcam, #ab154856, 1:500), anti-COXIV (Proteintech, #11242-1-AP, 1:500), anti-UCQCRC2 (Proteintech, #14742-1-AP, 1:500), anti-8OHdG (Santa Cruz, #393871, 1:100), anti-CD63 (Abcam, #ab8219, 1:100), anti-LBPA (Echelon Biosciences, #z-PLBPA, 1:500), anti-ALG2 (Proteintech, #12303-1-AP, 1:100). The following secondary antibodies were used for immunofluorescence analysis at 1:1000 dilution: Goat-anti-rabbit Alexa 647 (Invitrogen, # A21244), donkey-anti-rabbit Alexa 405 (Invitrogen, # A48258), goat-anti-rabbit Alexa 488 (Invitrogen, # A11011), goat-anti-mouse Alexa 488 (Invitrogen, # 11029), goat-anti-mouse Alexa 647 (Invitrogen, #A21235), goat-anti-rat Alexa 647 (Invitrogen, #A21247).
Validation	All the antibodies purchased have been validated in multiple previous studies accessible at the manufacturer's website. anti-TOM20 (Proteintech, #11802-1-AP) https://www.ptglab.com/products/TOM20-Antibody-11802-1-AP.htm anti-cytochrome C (Abcam, #ab110325) https://www.abcam.com/products/primary-antibodies/cytochrome-c-antibody-37ba11-ab110325.html anti-PDH (Abcam, #ab110333) https://www.abcam.com/products/primary-antibodies/pyruvate-dehydrogenase-e2e3bp-antibody-13g2ae2bh5-ab110333.html anti-Atp5L (Proteintech, #16483) https://www.ptglab.com/products/ATP5I-Antibody-16483-1-AP.htm anti-Atp5 (Abcam, #ab14748) https://www.abcam.com/products/primary-antibodies/atp5a-antibody-15h4c4-mitochondrial-marker-ab14748.html anti-VDAC1 (Abcam, #ab154856) https://www.abcam.com/products/primary-antibodies/vdac1porin--vdac2-antibody-epr10852b-mitochondrial-loading-control-ab154856.html anti-COXIV (Proteintech, #11242-1-AP) https://www.ptglab.com/products/COX4I1-Antibody-11242-1-AP.htm anti-UCQCRC2 (Proteintech, #14742-1-AP) https://www.ptglab.com/products/UQCRC2-Antibody-14742-1-AP.htm anti-8OHdG (Santa Cruz, #393871) https://www.scbt.com/p/8-ohdg-antibody-e-8 anti-CD63 (Abcam, #ab8219) https://www.abcam.com/products/primary-antibodies/cd63-antibody-mem-259-ab8219.html anti-LBPA (Echelon Biosciences, #z-PLBPA) https://www.echelon-inc.com/product/purified-mouse-anti-lbpa-bmp/ anti-ALG2 (Proteintech, #12303-1-AP) https://www.ptglab.com/products/PDCD6-Antibody-12303-1-AP.htm Goat-anti-rabbit Alexa 647 (Invitrogen, # A21244) https://www.thermofisher.com/antibody/product/Goat-anti-Rabbit-IgG-H-L-Cross-Adsorbed-Secondary-Antibody-Polyclonal/A-21244 Donkey-anti-rabbit Alexa 405 (Invitrogen, # A48258) https://www.thermofisher.com/antibody/product/Donkey-anti-Rabbit-IgG-H-L-Highly-Cross-Adsorbed-Secondary-Antibody-Polyclonal/A48258 Goat-anti-rabbit Alexa 488 (Invitrogen, # A11011) https://www.thermofisher.com/antibody/product/Goat-anti-Rabbit-IgG-H-L-Cross-Adsorbed-Secondary-Antibody-Polyclonal/A-11011 Goat-anti-mouse Alexa 488 (Invitrogen, # A11029) https://www.thermofisher.com/antibody/product/Goat-anti-Mouse-IgG-H-L-Highly-Cross-Adsorbed-Secondary-Antibody-Polyclonal/A-11029 Goat-anti-mouse Alexa 647 (Invitrogen, #A21235) https://www.thermofisher.com/antibody/product/Goat-anti-Mouse-IgG-H-L-Cross-Adsorbed-Secondary-Antibody-Polyclonal/A-21235 Goat-anti-rat Alexa 647 (Invitrogen, #A21247) https://www.thermofisher.com/antibody/product/Goat-anti-Rat-IgG-H-L-Cross-Adsorbed-Secondary-Antibody-Polyclonal/A-21247

Eukaryotic cell lines

Policy information about cell lines and Sex and Gender in Research

Cell line source(s)	AGS, HeLa, ModeK, Cos-1 and NCI-H292 were from ATCC. Drp1 KO and littermate WT MEFs, Parkin KO and littermate WT MEFs, Atg5 KO/Atg12KO/Atg14KO/Atg16KO and respective littermate WT controls have been previously described as indicated in the methods section. TRPML1 KO and littermate WT MEFs were generated for this study as described in the methods section
Authentication	Cells lines used in this study have different morphologies and growth characteristics. TRPML1 KO cells were authenticated by PCR as described in the methods section
Mycoplasma contamination	All cell lines utilized were free of mycoplasma

Commonly misidentified lines (See ICLAC register)	No ICLAC cell lines were used in this study

Plants

Seed stocks	N/A
Novel plant genotypes	N/A
Authentication	N/A